Shaping of membranes by arc-like particles

vorgelegt von
Master of Science
Francesco Bonazzi

von der Fakultät II - Mathematik und Naturwissenschaften
der Technischen Universität Berlin
zur Erlangung des akademischen Grades
Doktor der Naturwissenschaften
Dr.rer.nat.

genehmigte Dissertation

Promotionsausschuss:

Vorsitzender: Prof. Dr. Martin Schoen
Gutachterin: Prof. Dr. Sabine Klapp
Gutachter: Priv.-Doz. Dr. Thomas Weikl

Tag der wissenschaftlichen Aussprache: 14. Januar 2019

Berlin 2019

Abstract

This dissertation analyzes the interaction of biomembranes with arc-like particles, which gives rise to complex morphologies of organelles inside cells. The shaping of membranes is investigated with coarse-grained modeling and Monte Carlo simulations. In the coarse-grained model, the membrane is described as a discretized elastic surface, and the particles as segmented arcs.

Concave arc-like particles, i.e. particles interacting with the membrane on their concave side, shape membranes by inducing positive curvature at their binding sites. The membrane shape strongly depends on the overall angle and area concentration of the adsorbed particles. Particles with sufficiently large angles can induce both tubules and double-membrane disks, depending on their area concentrations. Double-membrane disks are stabilized by particles that adsorb only to the highly curved edges of the disks, while tubules are fully covered by particles.

If mixtures of both concave and convex particles are allowed to bind, morphologies with regions of negative curvature appear on the membrane. A frequently observed membrane morphology resembles a bulged ball, in which concave and convex particles create bulges and invaginations on the membrane, respectively. For small particles and low concentration of convex particles, U-shaped tubular and three-way junction morphologies are observed, which are common in the peripheral endoplasmic reticulum.

Finally, this dissertation shows that the membrane-mediated interaction between bound concave particles depends on the overall membrane curvature. The radial distribution function for bound particles is computed, and the membrane-mediated interaction between particles is derived with the reversible work theorem. Membrane curvatures that are compatible with the particle curvature have a weaker membrane-mediated interaction, which indicates that the induction of curvature on the membrane plays an important role for the membrane-mediated particle-particle interactions.

Zusammenfassung

Diese Dissertation analysiert die Wechselwirkung von Biomembranen mit bogenförmigen Partikeln, die zu komplexen Morphologien von Organellen innerhalb einer Zelle führen. Die Modellierung von Membranen wird mit vergröberten Modellen und Monte-Carlo-Simulationen untersucht. In dem vergröberten wird die Membran als eine diskretisierte, elastische Oberfläche und die Partikel als segmentierte Bögen beschrieben.

Konkave bogenartige Teilchen, d. h. Teilchen, die mit der Membran über ihre konkaven Seite wechselwirken, formen Membranen, indem sie eine positive Krümmung an ihren Bindungsstellen induzieren. Die Membranform hängt stark von dem Gesamtwinkel und der Flächenkonzentration der adsorbierten Teilchen ab. Teilchen mit ausreichend großen Winkeln können abhängig von ihren Flächenkonzentrationen sowohl Tubuli als auch diskoide Membranformen induzieren. Die diskoiden Formen werden durch Teilchen stabilisiert, die nur an den stark gekrümmten Rändern adsorbieren, während die Tubuli vollständig von Teilchen bedeckt sind.

Bei Mischungen von konkaven und konvexen Teilchen treten Morphologien auf, die Bereiche mit negativer Krümmung enthalten. Eine häufig zu beobachtende Membranmorphologie ähnelt einer gewölbten Kugel, bei der konkave und konvexe Teilchen Wölbungen und Invaginationen auf der Membran erzeugen. Für kleine Teilchen und geringe Konzentrationen von konvexen Teilchen kommt es zu U-förmigen tubulären Morphologien und tubulären Verzweigungen, die im peripheren Endoplasmatischen Retikulum vorkommen.

Schließlich zeigt diese Dissertation, dass die membranvermittelte Wechselwirkung zwischen gebundenen konkaven Teilchen von der globalen Membrankrümmung abhängt. Die radiale Verteilungsfunktion für gebundene Teilchen wird berechnet, und die membranvermittelte Wechselwirkung zwischen Teilchen wird mit dem Reversible Work Theorem abgeleitet. Membrankrümmungen, die mit der Krümmung der Teilchen kompatibel sind, weisen eine schwächere membranvermittelte Wechselwirkung auf, was darauf hindeutet, dass die induzierte Membrankrümmung eine wichtige Rolle für die membranvermittelten Teilchen-Teilchen-Wechselwirkungen spielt.

Contents

1. Introduction

Biological membranes are fundamental structures around and inside cells. The formation of membranes is regulated by the self-assembly of amphipathic lipids, which produces lipid bilayers. The bilayers self-assemble as a consequence of the hydrophobic interaction on amphipathic molecules: phospholipids are made of a hydrophilic head naturally attracted to water, while their hydrophobic tail tries to avoid water contact. The resulting self-assembly process allows the formation of a two-dimensional bilayer. The thickness of lipid bilayers is in the order of magnitude of nanometers, while their surface extent is usually in the order of micrometers.

Historically, it was a paper by Gorter and Grendel in 1925[19] to first hypothesize that membranes are composed of lipid bilayers. They came to this conclusion after observing a 2 to 1 ratio in the measurement of the surface areas with two different methods. Their model failed to include other molecules, such as proteins which were later included by Davson and Danielli, who had advanced doubts in 1935[10] on the single bilayer hypothesis for cellular membranes. Their model proposed that membranes are made of lipid bilayers with a double protein coating.

The modern understanding of biological membranes came only in 1972 when Singer and Nicolson introduced the fluid-mosaic model[53]. They started from the observation that proteins are able to move inside the membrane, evidence for a fluid state. This led to the conclusion that, in addition to lipids, the membrane is composed of cholesterol and proteins. Lipids are the principal component of the bilayer which, above their melting temperature, are in a fluid state, whereas proteins can be peripheral or integral with respect to the membrane. Integral membrane proteins contain parts, mostly hydrophobic helices, that are embedded in the lipid bilayer. Peripheral proteins are bound to the membrane, but are not embedded into the lipid bilayer.

1.1. Morphologies of biological membranes

Many biological membranes, especially inside cells, exhibit highly curved shapes[47, 26, 34], among which, as an example of interest, tubules and flattened sheets are recurrent patterns. The endoplasmic reticulum (ER) is an organelle inside eukaryotic cells containing both of these patterns in abundance[46]. Its inner part, known as the nuclear envelope, surrounds the cellular nucleus while the peripheral ER stretches to the whole cell. The ER is made of an interconnected network carved out of a single membrane, which exhibits abundance of both tubular and sheet-like patterns. Tubules are sections of membranes shaped into long cylindrical-like structures. They are most prominent in the peripheral endoplasmic reticulum[58], where they can form complicated structures,

such as densly packed tubular networks[34] as well as three-way junctions of tubules. The sheets on the other hand consist of a membrane flattened into two parallel flat surfaces connected at their ends by a highly curved edge. Inside the ER, sheets are usually located in the nuclear envelope[22], as helicoidal stack in the perinuclear region[14], and as flattened cisternal structures close to the plasma[15]. The diameter of the tubules and height of the sheets are both of the order of 50 nm in mammalian cells[42], which has led to the hypothesis of a common formation mechanism.

Lipid membranes have a natural tendency to minimize their curvature, as highly bent shapes are usually energetically unfavorable[62, 32]. Various mechanisms for the formation of highly curved membrane shapes are known, mostly involving interaction of the membrane with proteins. Many protein types are responsible for the membane shaping, for example BAR domains[54, 37], which are arc-like particles interacting with the membrane on their concave side, and reticulons[57]. Reticulons are able to oligomerize into arc-like scaffolds[48] and probably act similarly to BAR domains.

Sheets: It has been suggested that the strong curvature at the edge of the sheets is induced by the interaction with assemblies of proteins of the reticulon class and other similar ones[42]. Their structure has indeed interesting properties, such as hydrophobic hairpins, which could mold the membrane by shallow internalization into the lipid bilayer, and a semicircular arclike shape, exerting pressure on parts of the membrane.

It is known that other proteins act as stabilizers between the two parallel surfaces of an ER sheet by acting directly on them. Proteins like Climp63, p180, kineticin, and transcolon belong to this category[47]. In particular, experiments have shown that Climp63 causes a great abundance of sheets in the ER if overexpressed. On the other hand, the absence of Climp63 appears not to prevent the formation of sheet-like structures, rather causing the space separating the parallel surfaces of the sheets to shrink [60]. This leads to the suggestion that such classes of proteins act merely as helpers to the construction of the ER structures, but are not the unique builders.

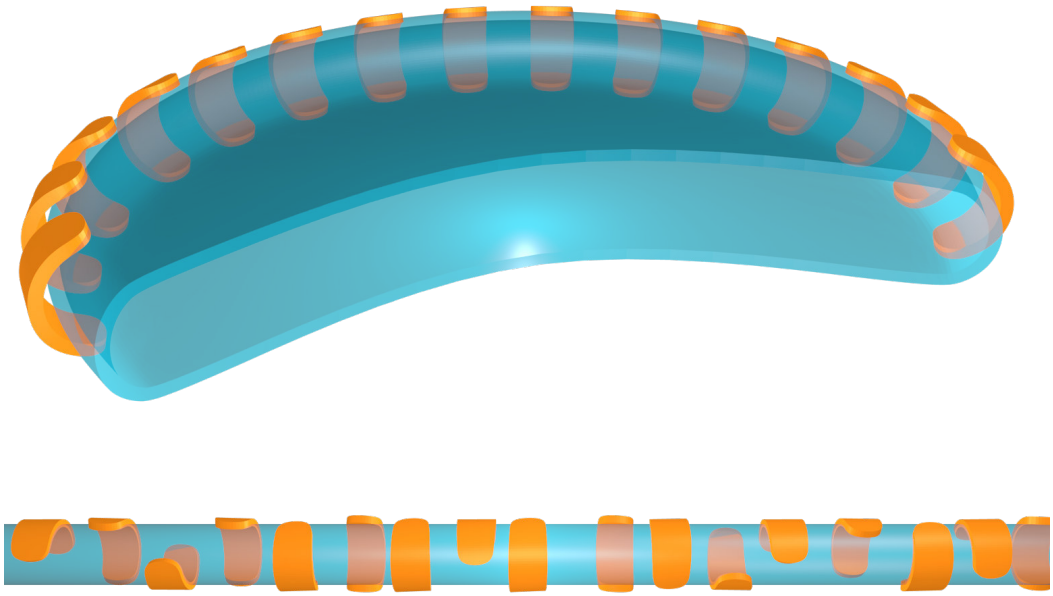

Figure 1.1.1.: Illustration of the scaffolding hypothesis, in the upper image the membrane has been shaped into a sheet of two parallel surfaces by an array of arc-like particles. In the lower image the particles have shaped the membrane into a tubule by surrounding its cylindrical side.

Tubules: Tubules occur frequently in cells, most notably in the peripheral ER. Tubules are known to be induced by arc-shaped proteins[17, 23]. Reticulons allow for the stabilization of tubules inside the ER and at the same time it is believed that they play a vital role in the stabilization of the edges of flattened sheets in the ER[34, 14].

Another class of proteins often associated with stabilizing tubular structures are N-BAR domains[37]. They are arc-shaped proteins with two domains containing amphipathic termini. First evidence from electron microscopy [33, 1, 17] indicated that N-BAR domains can form highly ordered helical coats around membrane tubules that are apparently held together by direct protein-protein interactions. Recent tomographic imaging of T-tubules[11], which are tubular structures found in skeletal and cardiac muscle cells, showed that Bin1 N-BAR domains form rather loose and irregular arrangements, possibly governed by weak or no direct interaction between neighboring proteins.

Apart from direct protein-protein interactions, the shaping by arc-shaped proteins induced on the membrane has a cost in terms of bending energy. Therefore, it has been suggested that energy minimization could be achieved by a close arrangement of such particles [13, 25, 61, 41, 59]. This effect has been shown to result in a membrane-mediated attractive force between proteins[41]. Other types of membrane-mediated interactions

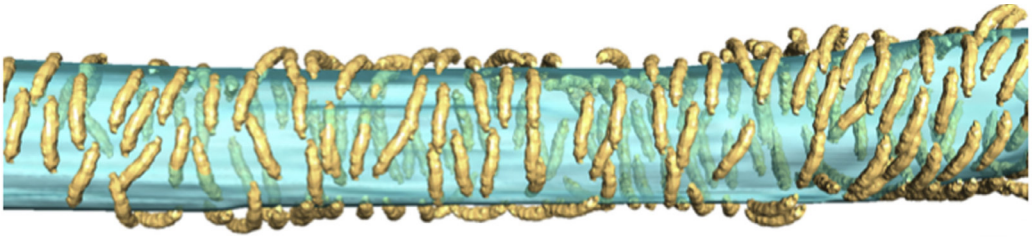

Figure 1.1.2.: Sub-tomogram of a T-tubule (blue) surrounded by Bin1 N-BAR domains (yellow), reproduced from Daum-Meister 2016[11] with permission (CC BY-NC-ND 4.0). It shows only short-range order, which suggests no direct protein-protein interactions.

are caused by the reduction in thermal fluctuations on the membrane, which may result in Casimir-like interactions between particles[52, 6, 20, 27].

3 way junctions: Three-way junctions are points of connection of three tubules often found in the peripheral endoplasmic reticulum[40]. Tubular structures in the ER are highly dynamic: they keep splitting and joining, ending up creating numerous 3-way junctions. At the same time the tubules forming 3-way junctions may shift along one another, possibly resulting in the destruction of the junction itself by separation of the tubule or by fusion of junctions.

According to a recent hypothesis, the formation of 3-way junctions is made possible by the Lunapark (Lnp1) protein[8, 9, 40]. Lnp1 is believed to act in concerted manner with the Yop1[9]. Experimental evidence of variation of the concentration of Lnp1 has shown that if Lnp1 is missing, the ER appears to collapse into a densely packed structure. On the other hand, an overexpression of Lnp1 causes a large amount of polygonal structures connected by 3-way junctions to appear[40].

Two transmembrane domains, the components of Lnp1, are likely shaped like a concave wedge, suggesting the possibility of inducing negative curvature on the membrane bound to Lnp1[8, 40], therefore acting in opposition to reticulons and BAR domains. Furthermore, multiple Lnp1 molecules may possibly form larger structures contributing to the formation and stabilization the 3-way junctions[8, 40].

1.2. Elastic energy of membranes

Lipid bilayers are self-assembled surface-like structures used as model systems for biological membranes. The hydrophobic interaction together with the amphipathic behavior makes phospholipids assemble in lipid bilayers. If the temperature is above the chain-melting temperature, as it is the case of interest in this project, the lipid bilayer has a two dimensional fluid nature.

There are two main types of membrane models: the molecular and the elastic ones. The molecular models are atomistic and coarse-grained, they involve representations of atoms in molecules or approximations thereof, with various degrees of discretization[16].

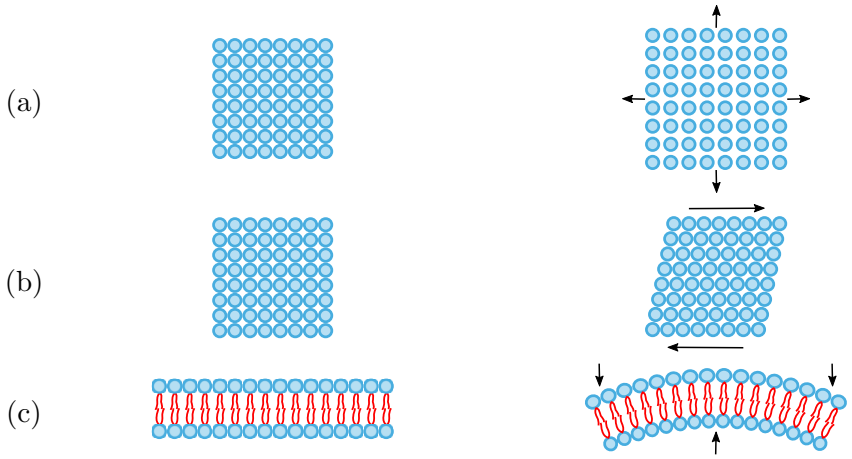

Figure 1.2.1.: Examples of elastic surface deformations acting on a lipid bilayer. Dilation force (a) stretches (or compresses) the membrane uniformly in all directions, while shearing (b) preserves the area. If the membrane is fluid, there will be no resistence to shearing. Bending forces of the membrane (c) act on the orthogonal direction to the surface.

These models are useful for simulations usually performed at small length and time scales. The elastic models, on the other hand, treat the membrane as a fluid, elastic sheet. They are suitable for larger membranes, as it is unfeasible to perform simulations at molecular level of detail with the current available computational technology. The most influential elastic model is due to Helfrich[21]. The triangulated membrane model is a discretization of Helfich's elastic membrane model.

The elastic models are justified by the fact that the lipid bilayer, once formed, acts in a similar manner to an elastic surface. Under this assumption the membrane may be handled with the classical elastic theory. In particular, the surface undergoes deformations due to bending, stretching and shearing, as illustrated in figure 1.2.1. The shearing forces may be ignored, as the membrane is fluid and therefore any force resisting the relocation of molecules in space is nonexistent. The hydrophobically-induced attraction between phospholipidic tails is pretty strong, therefore any stretching force acting on the membrane has minimal effects and fluid membranes are nearly incompressible[29]. This condition can be modeled by subjecting the area to the harmonic potential around an equilibrium surface area

$$U_{\text{stretching}} \propto \Delta A^2, \tag{1.2.1}$$

where $\Delta A = A - \bar{A}$ represents the membrane area A as displaced from the equilibrium area $\bar{A}$.

The bending modeling is more complex and requires the introduction of concepts from differential geometry. Mathematical surfaces in space are regarded as two dimensional differential manifolds embedded in the $\mathbb{R}^3$ space. There are various ways to represent them mathematically, for example with a map $f : \mathbb{R}^2 \to \mathbb{R}^3$ from the local coordinates of

the surface to the corresponding position in space (arguments about the existence of such mapping, which usually holds, are neglected for simplicity). The curvature of a curve on the surface passing through a point is the reciprocal of the radius of the osculating circle tangent to that curve at that point. The principal curvatures C_1 and C_2 at a point of the surface are the curvatures of two curves, orthogonal to each other, whose values are the extrema of all curvatures of the curves passing through that point. A theorem by Gauss guarantees the existence of the principal curvatures. Furthermore, the principal curvatures are invariants as they do not depend on the chosen parametrization. The principal curvatures are used to build the mean curvature

$$H = \frac{1}{2}(C_1 + C_2) \tag{1.2.2}$$

and the Gaussian curvature[45]:

$$K = C_1 C_2 \tag{1.2.3}$$

The bending energy of the surface may be calculated as a surface integral[21]. As the bending energy is a physical property and therefore has to be independent of the parametrization, the bending energy can be expressed as a function of invariants only. The integral may therefore be expanded up to the second Taylor term as

$$\beta E_{\text{bending}} = \int \Big[2\kappa(M - M_{\text{sp}})^2 + \bar{\kappa}K\Big] dA \tag{1.2.4}$$

where M and K are the total and Gaussian curvatures, as previously defined. The bending rigidity κ is a constant that characterizes the rigidity of the membrane, in biological membranes it is usually in the order of $10 - 40kT$[59]. The variable $\bar{\kappa}$ is the modulus of the Gaussian curvature and is supposed to be in the same order of magnitude as the bending rigidity $\kappa \approx \bar{\kappa}$[43], β is the inverted beta $\beta = \frac{1}{k_B T}$, and, lastly, the spontaneous curvature H_{sp} is used to quantify the tendency of the membrane to naturally bend on one side, usually due to asymmetricity in the composition between the two layers. Expression 1.2.4 gives a good approximation of the bending energy of a real lipid bilayer, provided that its thickness is small compared to its radius of curvature[62].

Only membranes of spherical topology are relevant to this research project, that is membranes having a shape that can be continuously deformed into a sphere (membranes without holes and without topological foldings such as in the Klein bottle). As a consequence of Gauss-Bonnet theorem[28] the integral over the Gaussian curvature K gives a constant contribution to the total energy for fixed topology, and may therefore be omitted. Furthermore, in this project the two layers of the membrane are assumed to be symmetric, the consequence of dropping the spontaneous curvature term. As a last reminder, equation 1.2.4 has a linear dependence between β and κ. These units can be chosen so that β gets absorbed into κ. It is reasonable to operate on β units (such that $kT = 1$) and employ the value $\kappa = 10$. The energy expression may be rewritten as

$$E_{\text{bending}} = \int 2\kappa M^2 \, dA \,, \tag{1.2.5}$$

2. Model and methods

In this chapter, a model for particles interacting with a triangulated membrane is proposed. The triangulated membrane is a discretization suitable for computer simulations of the continuous elastic model of equation 1.2.5. Particles interacting with the triangulated surface are then introduced.

2.1. Model

2.1.1. Triangulated membranes

The integral expression 1.2.5 can be approximated in a standardized way by a summation over a triangulated surface[5, 24], which can be used in computer simulations. The mathematical surface is therefore replaced by a large polyhedron of triangular faces. The number of vertices n_V, of edges n_E and of triangles n_T are constant values and obey the topological constraint

$$n_V - n_E + n_T = \chi = 2,$$

where χ is known as Euler characteristic. The value $\chi = 2$ is the condition for the topology of the sphere, that is, a surface with neither holes nor foldings.

Geometrical properties of the membrane

Given a triangulation, geometrical quantities such as the surface area and the volume in the enclosed space can be calculated from its geometrical elements. For instance, the

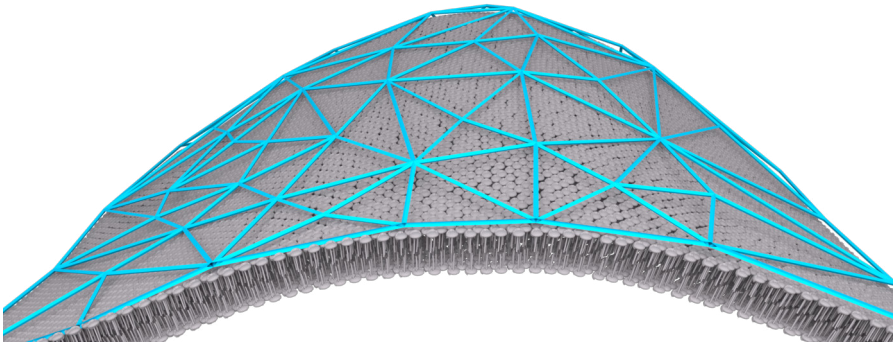

Figure 2.1.1.: Illustration of a lipid bilayer and a corresponding triangulated surface.

membrane surface area is the sum of the areas of all triangles on the triangulation. It is given by

$$A = \frac{1}{2}\sum_{i\in F} |\mathbf{e}_{i,1} \times \mathbf{e}_{i,2}| = \frac{1}{2}\sum_{i\in F} l_{i,1} l_{i,2} \sin\theta_{i,12} \tag{2.1.1}$$

where the summation runs over all triangles. The vectors $\mathbf{e}_{i,1}$ and $\mathbf{e}_{i,2}$ are any two of the three edges of triangle i and $l_{i,j}$ is the length of $\mathbf{e}_{i,j}$.

In an analogous way, the volume of the space enclosed by the membrane is determined by a summation of all signed tetrahedron volumes over all triangles

$$V = \frac{1}{6}\sum_{i\in F} \mathbf{v}_{i,1} \cdot (\mathbf{v}_{i,2} \times \mathbf{v}_{i,3}),$$

where $\mathbf{v}_{i,j}$ is the vector representing the position in space of the j-th vertex of triangle i.

The reduced volume is then introduced as[44]

$$v = 6\sqrt{\pi}\frac{V}{A^{\frac{3}{2}}} \leq 1, \tag{2.1.2}$$

where V is the volume of the space inside the membrane and A is the surface area of the membrane. The reduced volume is a dimensionless quantity which is proportional to the volume of the space enclosed by the membrane if the surface area is kept constant. The reduced volume is in the $0 < v \leq 1$ range depending on the shape of the membrane. The sphere maximizes the value of the reduced volume to unity.

Ideally, the triangles of the triangulated membrane should be shaped as close as possible to equilateral triangles and not differ much in area. If all triangles were equilateral triangles (which is almost always geometrically impossible to fit), the edge length would be

$$a_E = \sqrt{\frac{4A}{\sqrt{3}n_F}} \tag{2.1.3}$$

The edges of triangles are subjected to a tether potential limiting their lengths to a specific range. The minimal edge length is set to be 20% less than a_E

$$a_m := \frac{4}{5}a_E \tag{2.1.4}$$

while the maximum edge length is $\sqrt{3}a_m$. Therefore the edges of the triangulated surface are then subjected to a tether potential keeping their lengths in the $l \in [a_m, \sqrt{3}a_m]$ range[24, 5]. This choice allows the shapes and areas of the membrane triangles to cover the majority of triangular shapes, with the exclusion of very thin ones. From now on, a_m will be used as the reference unit.

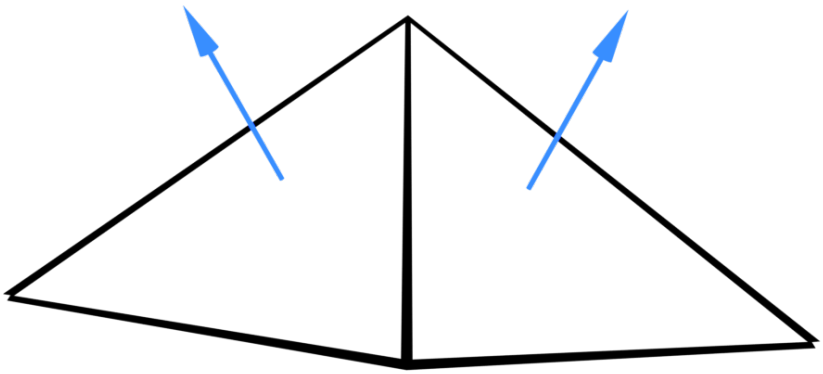

Figure 2.1.2.: Illustration of two adjacent triangles of area $A_i$and A_j on a triangulated surface. Their shared edge has length l_{ij} and their normal unit vectors $\mathbf{n}_i$ and $\mathbf{n}_j$ are shown. The dihedral angle ϕ_{ij} between the planes identified by the two triangles is related to the normals of the triangles by the relation $\cos\phi_{ij} = \mathbf{n}_i \cdot \mathbf{n}_j$.

Bending energy of a triangulated membrane

The elastic energy of the membrane is calculated through an approximation on the triangles of Helfrich's integral for the bending energy, summed over the vertices[24]

$$E_{\text{bending}} = 2\kappa \sum_{\alpha=1}^{n_V} \frac{M_\alpha^2}{A_\alpha}, \tag{2.1.5}$$

where M_α is the average contribution to the curvature of vertex α. Its expression is[24]

$$M_\alpha = \frac{1}{4} \sum_{(ij)} l_{ij}\phi_{ij}\,,$$

where the summation ranges over all edges ij that share vertex α. The variable l_{ij} denotes the length of the edge, while ϕ_{ij} is the dihedral angle between the triangles i and j adjacent to the edge. The area associated to the vertex is $A_\alpha = \frac{1}{3}\sum_i A_i$, where the summation, as before, runs over the three triangles that share the vertex α. The bending rigidity is generically measured to be around $\kappa \approx 10 - 40 k_B T$ for lipid bilayers, where $k_B T$ is the thermal energy[59]. A reasonable value for the bending rigidity is $\kappa = 10\ k_B T$[12]. The vertices of the membrane are allowed to fluctuate, while the edges connecting them can be flipped and connected to other neighboring vertices, ensuring membrane fluidity[18].

Dilations in triangulated membranes

Fluid membranes are nearly incompressible (cfr. equation 1.2.1). As a consequence, if the amount of lipids does not vary, the total surface area of the membrane does not vary. This is modeled by subjecting the membrane surface area to the harmonic potential of equation 1.2.1, as

$$U_{\text{stretching}} = c_B(A - A_0)^2 \tag{2.1.6}$$

Here, c_B is the stretching constant, A is the observed area of the membrane 2.1.1. A_0 is a fixed area value kept at $A_0 \approx 0.677 n_T a_m^2$, which is the area minimizing the stretching energy. In this project the value of c_B has been calibrated to limit the fluctuations of the area by around 1%. The suitable value of

$$c_B = 2 \cdot 10^5 \left[\frac{1}{\beta V_{\text{ref}}^{\frac{2}{3}}} \right] \tag{2.1.7}$$

has been used.

Volume potential

In certain cases, the membrane volume may be constrained to a certain value, which causes the membrane to be shaped into tubular or spherical morphology[4]. The additional energy contribution is

$$E_V = c_V \left(v - v_0\right)^2, \tag{2.1.8}$$

where v is the volume of the space enclosed by the membrane (see equation 2.1.2), v_0 is the desired reduced volume and $c_V = 2 \cdot 10^5$ is chosen so that the variation of the volume is less than 1%. For simulations where the volume inside the membrane is allowed to freely fluctuate, the value of c_V is zero.

2.1.2. Particles

Membrane-shaping particles such as BAR-domains[54, 37] or reticulons[57] are arc-shaped. Their shape allows them to exert bending force by lightly binding to the membrane. Proteins or protein oligomers are modeled in this project as rigid bodies. These particles are composed of a line of 3 to 7 contiguous quadratic segments of area a_p^2, where

$$a_p = \frac{3}{2} a_m.$$

Neighboring segments are curved 30° with respect to each other, giving the particle an arc-like shape. As the value of a_p is larger than the average edge length of a membrane triangle, different segments bind to different triangles on the membrane. The angle θ_d between adjacent segments is set to be 30°. As these particles are rigid bodies, the relative angles and distances between their segments will remain constants. Furthermore two particles may not occupy the same space nor overlap nor penetrate the membrane.

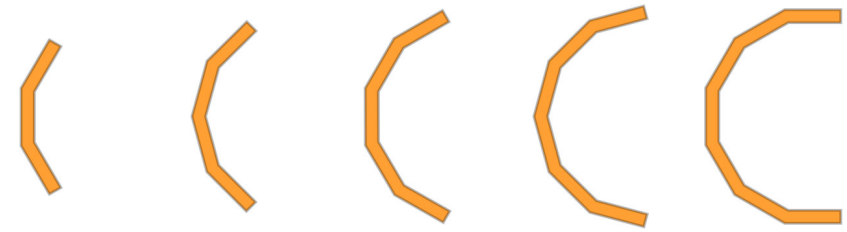

Figure 2.1.3.: Concave particles are finite sequences of 3, 4, 5, 6, 7 segments (orange). The angle between the extremal segments are 60°, 90, 120°, 150°, 180° respectively. Larger particles are expected to induce larger curvature on the membrane.

Following this definition, all particles possess the same curvature, which can be estimated by the radius of the cylindrical section comprising the centers of segments:

$$R_p = \frac{a_p}{2\tan\left(\frac{\theta_d}{2}\right)} \tag{2.1.9}$$

2.1.3. Particle-particle interaction

A hard-core repulsion between particles is introduced to avoid overlapping. Specifically, the hard-core repulsion is expressed by the interaction energy among segments with centers at $\mathbf{p}_1$ and $\mathbf{p}_2$ as

$$V_{pp} = \begin{cases} 0 & \text{if } |\mathbf{p}_1 - \mathbf{p}_2| > a_p \\ \infty & \text{otherwise} \end{cases} \tag{2.1.10}$$

As a result of this interaction, the segments behave like hard-spheres of radius $a_p/2$, with the exception of the interaction with the membrane, which is differently defined.

2.1.4. Membrane-particle potential

Every segment of a particle interacts with the closest triangle on the membrane surface with membrane-particle adhesion potential

$$V = -U \sum_{i \in S} f_r(r_i) f_\theta(\theta_i), \tag{2.1.11}$$

where S is the set of all particle segments, r_i is the distance between the center of segment i and the center of the nearest triangle on the membrane, θ_i is the supplementary angle to the angle between the normals of segment i and the nearest triangle. Two types of particles are considered, depending on the direction of their normals. If the normals of the particle segment point towards their curvature center, the particles are called concave and induce positive curvature on the membrane, causing protrusions on it, see

figure 2.1.4(a). Convex particles, on the contrary, have their segment normals pointing away from the center of curvature and induce negative curvature or invaginations on the membrane, see figure 2.1.4(b). By convention, the normals of the membrane triangles point outward from the enclosed volume. f_r and f_θ are properly chosen square-well potentials:

$$f_r(r) = \begin{cases} 1 & \text{if } r_1 < r < r_2 \\ 0 & \text{otherwise} \end{cases} \tag{2.1.12}$$

$$f_\theta(\theta) = \begin{cases} 1 & \text{if } |\theta| < \theta_c \\ 0 & \text{otherwise} \end{cases} \tag{2.1.13}$$

The parameters r_1, r_2, θ_c regulate the interaction configurations of the particle to the membrane. The values used in the simulations carried out in this project are $r_1 = \frac{1}{4}a_m$ and $r_2 = \frac{3}{4}a_m$. The angle threshold $\theta_c = 10°$ is used, unless differently stated. The variable U is the adhesion energy for the particle-membrane interaction.

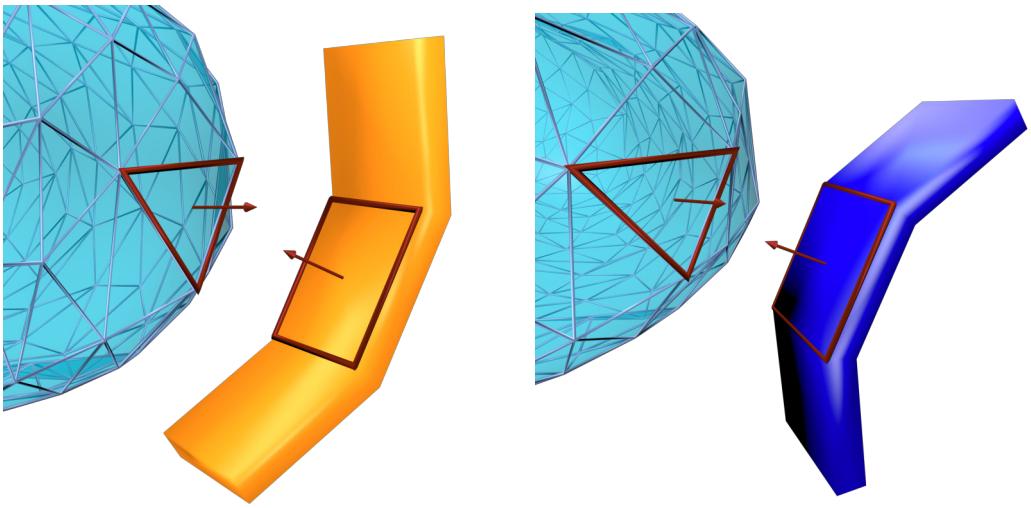

(a) (b)

Figure 2.1.4.: Illustration of two particle types and the mode of interaction with the membrane. The displayed vectors, along with the distance between triangle and square segment centers, determine the membrane-particle interaction. The (orange) concave particles (a) induce positive membrane curvature, as their normal vectors point towards the curvature center of the particle. Particles interacting on their convex side (b) are colored blue, they induce negative membrane curvature.

Coverage area on the membrane

The overlap of particles is prevented by the repulsive forces defined in equation 2.1.10. Every bound segment of a particle thus covers a surface area equal to

$$\pi \frac{a_p^2}{4} \tag{2.1.14}$$

on the membrane. Therefore the area fraction of the membrane covered by all bound particles is given by

$$x_{\text{coverage}} = \frac{n_B a_p^2 \pi}{4 A_m} \tag{2.1.15}$$

where n_B is the number of particle segments bound to the membrane triangles, A_m is the membrane area.

Anti-internalization algorithm

Particles are not allowed to enter the enclosed volume of the membrane. This can be encoded in the simulation software by setting the condition that the vector pointing from the membrane triangle to the particle segment must leave the membrane. Mathematically, this can be defined as

$$(\mathbf{p}_i - \mathbf{f}_j) \cdot \mathbf{n}_j^F > 0$$

where $\mathbf{p}_i$ is the position of the segment i, $\mathbf{f}_j$ is the position of the center of triangle j in a neighborhood up to distance $3 - 4\,a_m$ to the particle, and $\mathbf{n}_j^F$ is the normal vector of triangle j, pointing outward from the enclosed membrane volume.

2.2. Simulation methods

All simulations take place in a cubic box with periodic boundary conditions. The size of the box is given by

$$3V_{\text{ref}}^{\frac{1}{3}} \approx 50 a_m. \tag{2.2.1}$$

For each simulation, a single connected membrane is present in the box, typically with a reservoir of many fluctuating particles. The particles can be divided into bound and unbound states.

Metropolis Monte Carlo methods are employed in this project, whereby the evolution of the system is generated by random processes. The time evolution in the simulations relies on a Markov chain sampling of the Boltzmann distribution of energies through the Metropolis-Hastings algorithm. This means that the system will undergo test random state changes $E \longrightarrow E'$, with acceptance probability given by

$$P(E \longrightarrow E') = \min\{\exp(-\beta \Delta E), 1\},$$

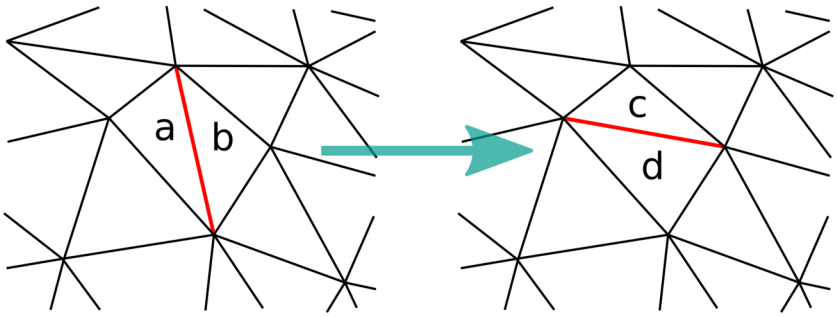

Figure 2.2.1.: Illustration of the edge flipping transformation. A triangulation edge is removed (left) and a new one is drawn (right) connecting the opposite vertices of the adjacent triangles a and b. As a result, triangles c and d are formed. This kind of transformation is needed to simulate the membrane fluidity.

where E is the energy of the current state, E' is the energy of the new state after a random change and $\Delta E = E' - E$ is the increase in energy. Notice that the random change is always accepted in case of a decrease in energy. The simulation consists of four different types of steps, randomly extracted each time with equal probability: vertex translations, edge flipping, particle translation and particle rotation.

Translations Translations are possible changes in the position of particles and membrane vertices. For vertex translations, a vertex is drawn randomly with all vertices being equally likely to be chosen. The same uniformity of probability applies to edges and particles. The maximum extent of translations and rotations is chosen such that the acceptance ratio is close to $\frac{1}{2}$. Given the maximum extent of translation $t_V^{\max}$ for the vertex move, the translation vector is limited by the condition $t_x, t_y, t_z \in [-t_v^{\max}, t_v^{\max}]$, with uniform probability in the interval. The same argument applies to particle translations, with maximum extent $t_P^{\max}$. The values $t_V^{\max} = \frac{1}{10} a_m$ and $t_P^{\max} = a_m$ are used in this project.

Edge flipping Edge flipping is a move by which an edge E is removed and the opposite vertices of the triangles adjacent to edge E are reconnected, as displayed in figure 2.2.1. The edges to flip are chosen uniformly from all edges in the triangulated membrane. This operation is required to assure that the membrane behaves like a two dimensional fluid, which is the state of biological membranes in cells.

Rotations The rotation axis passes through the central point along the particle arc. That is, the rotation axis passes through the middle point on the arc formed by the segment centers. In particular, for particles with odd numbers of segments the rotation axis passes through the center of the central segment. The maximum rotational angle

is tuned to around 3 to 4 degrees. For further details on the implementation, confer to A.2.

Averaging of simulation results The observed variables are measured at periodic time intervals throughout the simulation run. These intervals contain on average 10^6 vertex moves for each vertex. The average values of the observables are taken to be the arithmetic average of the last 10 measurements.

2.2.1. Initial configurations for the membrane

Every simulation is started with a single membrane of either $n_V = 1002$ vertices, $n_E = 3000$ edges and $n_T = 2000$ triangles or $n_V = 2562$ vertices, $n_E =$ edges and $n_T = 5120$ triangles. The smaller membrane of $n_T = 2000$ triangles has been shaped into three different initial configurations (sphere, disk, spherocylinder, see figure 2.2.2a) while the larger membrane has also been shaped into a three-way junction. The purpose of multiple initial configurations for the same parameters is to identify stable and metastable states and to investigate their convergences. In principle, sufficiently long simulations starting with different initial membrane shapes should converge to the same final equilibrium membrane shape if both simulations have the same parameters, for example the number of total particles and interaction strength U. Actual simulations are not always long enough for convergence to occur, especially with larger particles. In particular, the configurations used in this project are:

Sphere The sphere can be described by the surface

$$x^2 + y^2 + z^2 = R^2 \tag{2.2.2}$$

where R is its radius. The reduced volume of the sphere is equal to one, which is the largest value of reduced volumes among all possible shapes.

Ideal disk The ideal disk is composed of a low and thick cylinder and an outer semi-torus on its curved side. The ideal disk is described by two parameters: R, the radius of the cylinder, and r, the inner radius of the torus. The equations delimiting the disk are

$$\begin{cases} |z| < r & \text{if } x^2 + y^2 < R^2 \\ \left(\sqrt{x^2 + y^2} - R\right)^2 + z^2 = r^2 & \text{otherwise} \end{cases}. \tag{2.2.3}$$

The disk with $n_T = 2000$ employed as starting configuration has a reduced volume of 0.5252. The radius of curvature of the disk edge is chosen to be the particle curvature $R = r_p$ as defined in A.1.1, which is compatible with the curvature of the particles.

Ideal spherocylinder An ideal spherocylinder is a cylinder capped by two semi-spheres on its flat sides. The spherocylinder is a cylinder of radius r and height h capped by two semispheres on its flat sides. The equations for the spherocylinder are

$$\begin{cases} x^2 + y^2 = r^2 & \text{if } |z| < h \\ x^2 + y^2 + (z-h)^2 & \text{otherwise} \end{cases}. \tag{2.2.4}$$

Once formed, the spherocylinder with $n_T = 2000$ employed as starting configuration has a reduced volume of 0.3754. The radius of the spherocylinder is chosen to be $r = r_p$ from the definition A.1.1, compatible with the radius of curvature of the particles.

Three-way junction The three-way junction is a particular morphology connecting three tubules at a single junction. The three-way junction used as starting shape is created by shaping three semi-spherocylinders on a plane, whose axes are rotated by 120° with respect to one another. This starting morphology has been created for a membrane with $n_T = 5120$ only, see figure 2.2.2b. For practical purposes the radius of the three semi-spherocylinders constituting the junction is larger than r_p.

2.2.2. Starting configurations

Starting particle configurations for the membrane in the disk and for the spherocylinder shapes with bound particles have been used. In first place, simulations with frozen membrane moves have been run, allowing enough particles to eventually bind to the membrane. The resulting states are shown in figures 2.2.3(a) and 2.2.3(b). As soon as enough particles are bound, the full simulation with the membrane dynamics is started from that given state. For simulations starting with a spherical membrane shape, notice that no particles were bound to the membrane at the start of the full simulation.

2.2.3. Convergence criteria

In order to determine whether a simulation run has entered a stable or a meta-stable state, two variables are observed: the number of bound particles and the reduced volume. The last 10^7 MC steps per vertex of the simulation are divided into ten intervals of 10^6 steps, and the averages of the number of bound particles and reduced volume are calculated for these intervals. The simulations are considered converged if the standard deviation of the averages of the ten intervals are below 0.2 for both the number of bound particles and the reduced volume.

2.2.4. Cell list

In order to increase the speed of the simulation, it is necessary to make sure that interactions between different objects are only calculated with neighboring objects, thus avoiding spending computational time on the interaction energy between distant objects, whose value is certainly null. The cell list is a useful data structure to quickly locate

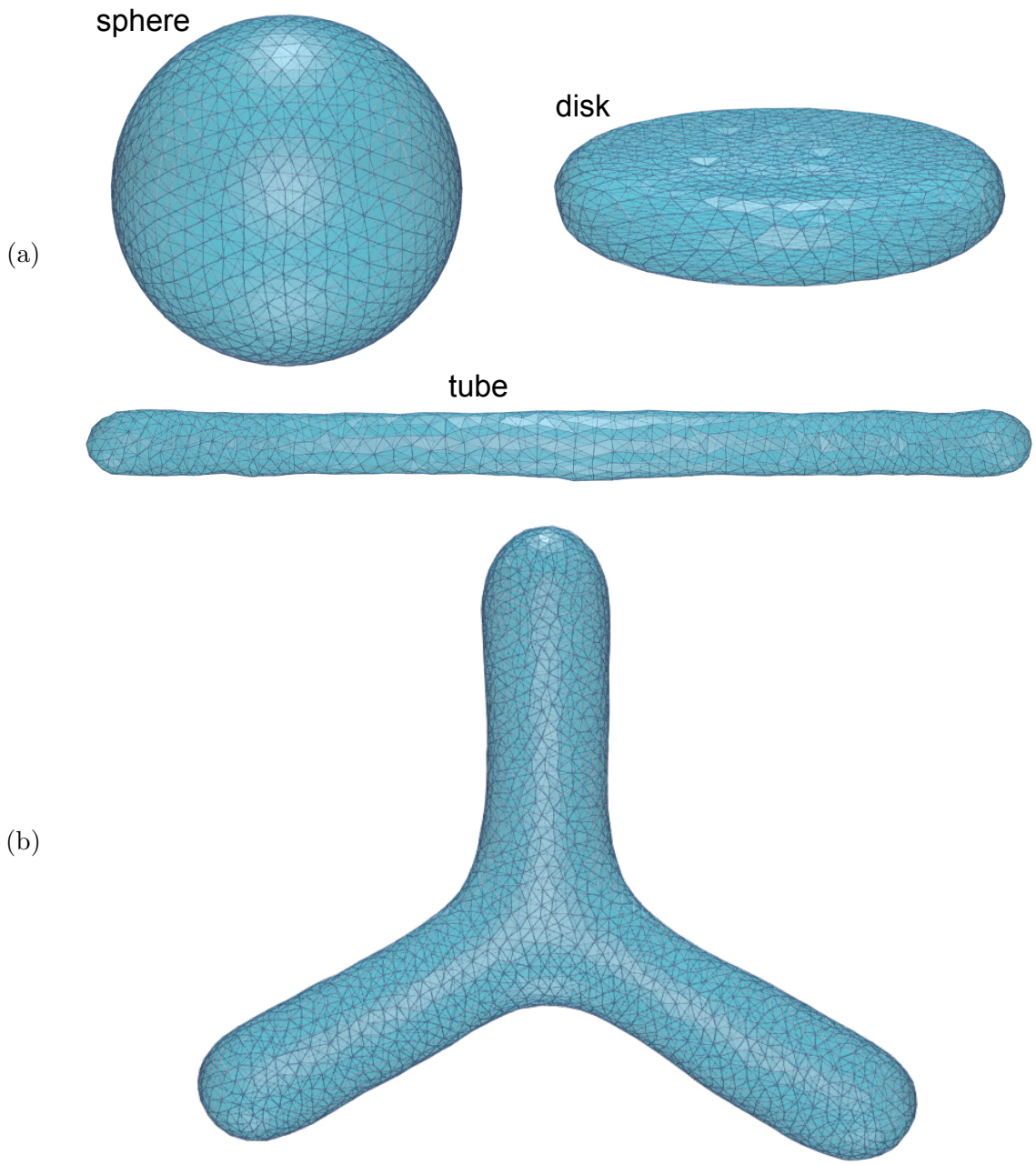

Figure 2.2.2.: Initial configurations for the membrane in the simulations performed in this project, no bound particles are shown in this picture. The membrane with $n_T = 2000$ triangles has been shaped into three configurations (a): the disk, the sphere and the spherocylinder. For the larger membrane of $n_T = 5120$ triangles an additional starting morphology (b) has been introduced in simulations with convex particles: the three-way junction.

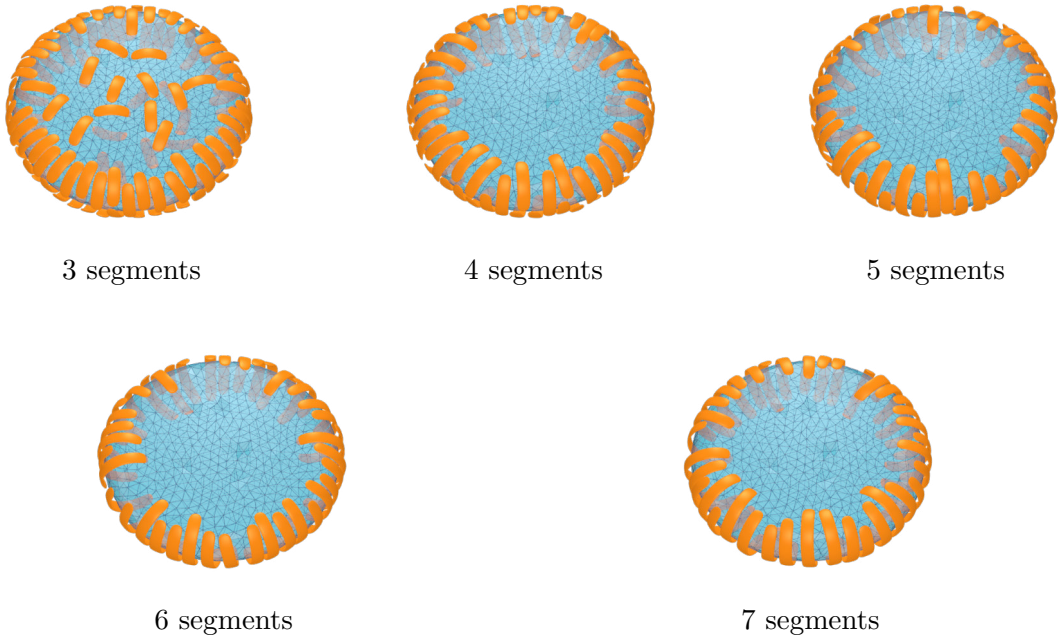

(a)

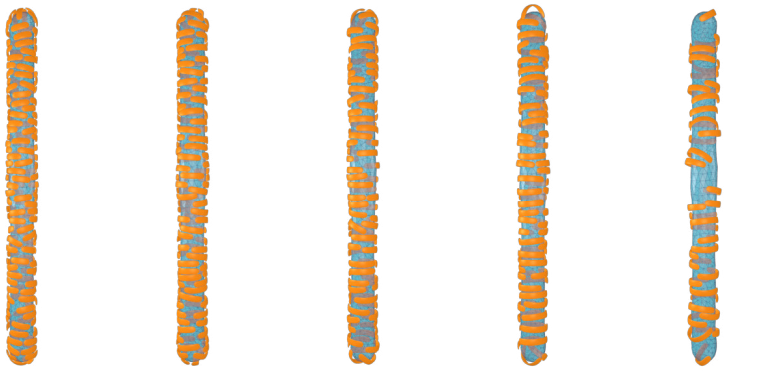

(b)

Figure 2.2.3.: Initial configurations for a membrane with $n_T = 2000$ triangles. In 2.2.3(a) the membrane has been shaped into a disk, while in 2.2.3(b) the shape is a spherocylinder. The sizes of particles range from 3 to 7.

neighboring particles: the space axes are divided in N equal intervals, thus identifying N^3 cubes. At this point, it is possible to create a list of N^3 elements, with each element representing a box containing the indexes for the objects lying within the boundary of that box.

Two such lists, indexing the triangles of the membrane and the segments of the particles, have been employed. Following the particle move, a search occurs to find all neighboring triangles, with the purpose of verifying that no particle internalization into the membrane occurs. After a vertex movement or an edge flip, all neighboring segments are looked up, so as to perform the same interaction calculation.

3. Shaping of membranes by concave particles

In this chapter, the model proposed in chapter 2 is applied to investigate the recurrent morphological structures of flattened sheets and tubules induced by concave particles. Concave particles can be interpreted as a model for the discretization of proteins forming scaffolds around membranes. The investigation is carried out with a triangulated membrane surrounded by concave particles. The simulations have been performed with $N = 200$ or $N = 400$ concave particles of size 3 to 7. The membrane with $n_T = 2000$ triangles is used in this chapter, and as starting configurations the sphere, the disk and the spherocylinder, with bound particles have been used. During the simulations, shape transitions may occur so that the converged membrane morphologies may be classified as fluctuating spheres, tubules, disks. In the case of particles with 4 segments, a fourth additional morphology has been observed, where the adsorbed particles are arranged in rows dividing the membrane into flat regions. This configuration is referred to as faceted membrane. In this chapter the constraint of equation 2.1.8 on the volume V of the space enclosed by the membrane is not enforced, or, equivalently, the constant of the volume energy is set to $c_V = 0$. Additionally the bending rigidity of the membrane is $\kappa = 10 k_B T$ for all simulations.

3.1. Angles induced by particles

Concave particles of 3 to 7 segments are illustrated in figure 3.1.1(a). These particles induce curvature on the membrane by binding on their concave side, as schematically visualized in figure 3.1.2. Each particle segment binds to only one membrane triangle, with the range of angles for the triangle normals determined by equation 2.1.13. The distribution of angles between the normals of the triangles bound to the first and last particle segments may be used to quantify the induced curvature on the membrane. The distributions for particles of size 3 to 7 and $\theta_c = 10°$ are shown in Figure 3.1.1(b). Similarly, figure 3.1.1(c) compares the same distributions for values $\theta_c = 3°, 5°, 10°$ with particles of size 3. The graph shows that larger particles are able to induce higher curvatures on the membrane. Lower values for θ_c decrease the distribution variance and slightly increase the mean induced angles.

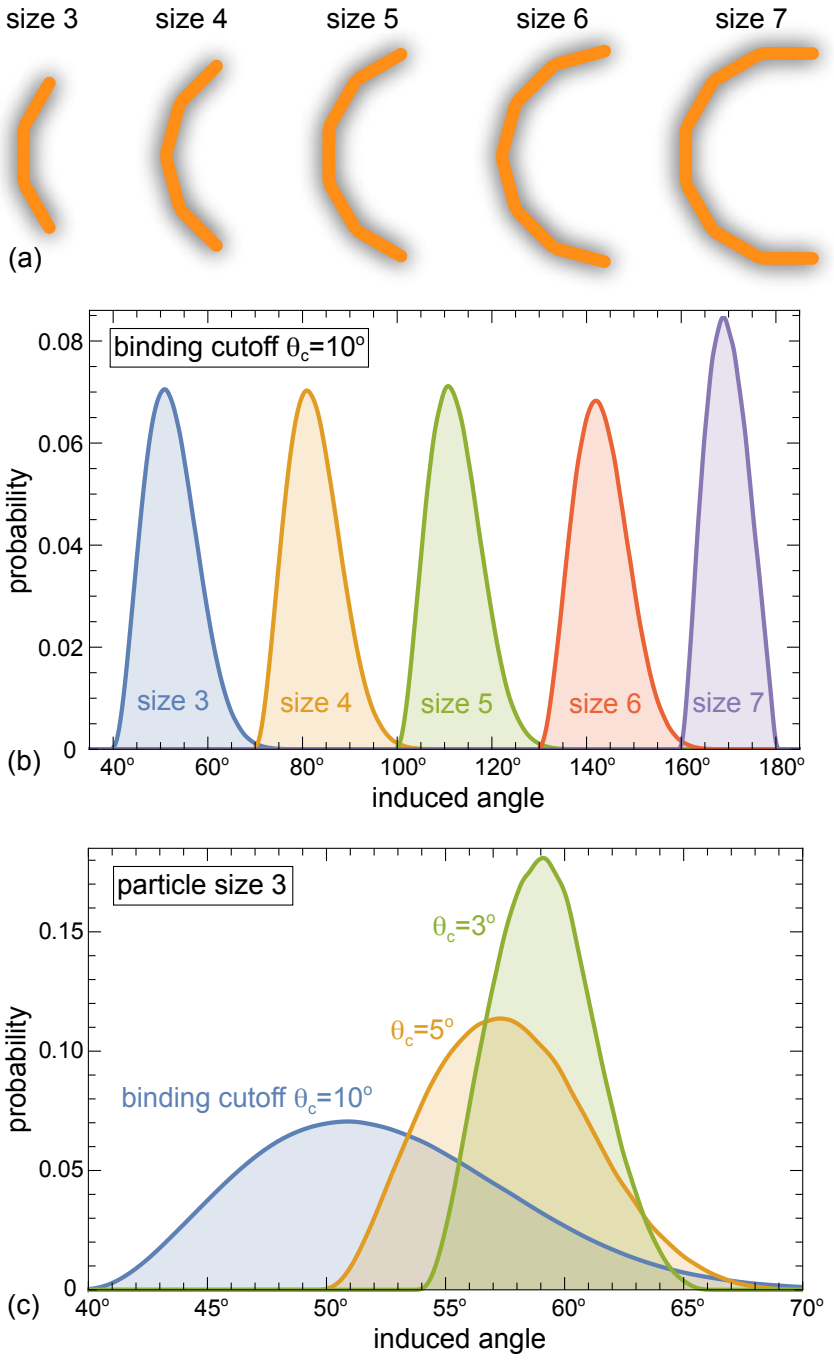

Figure 3.1.1.: Distributions of angles induced by particles of various sizes. The angular aperture induced by a bound particle is calculated as the angle between the normal vectors of the two triangles of the membrane interacting with the first and last square of said particle.

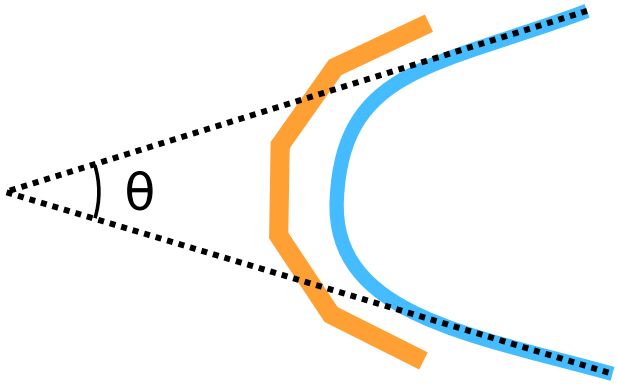

Figure 3.1.2.: Illustration of the estimated angle induced by a particle (orange) on the membrane (blue). The angle θ is generally smaller than the angle formed by the extremal segments of the particle.

3.2. Membrane morphologies

Figure 3.2.1 displays, for every particle size and value of θ_c, a plot of the converged simulations along the membrane coverage and reduced volume. The points represent simulations starting from different initial membrane shapes and parameters, like the adhesion constant U and number of concave particles N. The resulting morphologies are classified as spherical, disk-like, tubular and faceted and the simulations are colored accordingly. Simulations with the same parameters sometimes converge to different shapes, which indicates metastabilities. Nevertheless, the plots show that the simulations are located along curves, irrespective of stability or metastability. This implies that the reduced volume may be considered as a function of the membrane coverage for a given particle size and angle cutoff θ_c, therefore also the morphology is determined by the membrane coverage.

Metastabilities

Simulations starting from different initial configurations do not always reproduce all kinds of final states by varying adhesion energy and particle number. This indicates that converged states may be metastable. In particular, for particles of size 3, 4, and 5 the simulations starting from a spherical morphology are able to reproduce all final states, while for larger particles, that is of sizes 6 and 7, no tubular or discoidal morphologies emerge.

Phases and particle sizes

For particles of three segments, different simulations with angle cutoff $\theta_c = 3°, 5°, 10°$ have been performed. The equilibrium configurations of the membrane for particles of three segments have been classified into two states, the fluctuating sphere and the tubule.

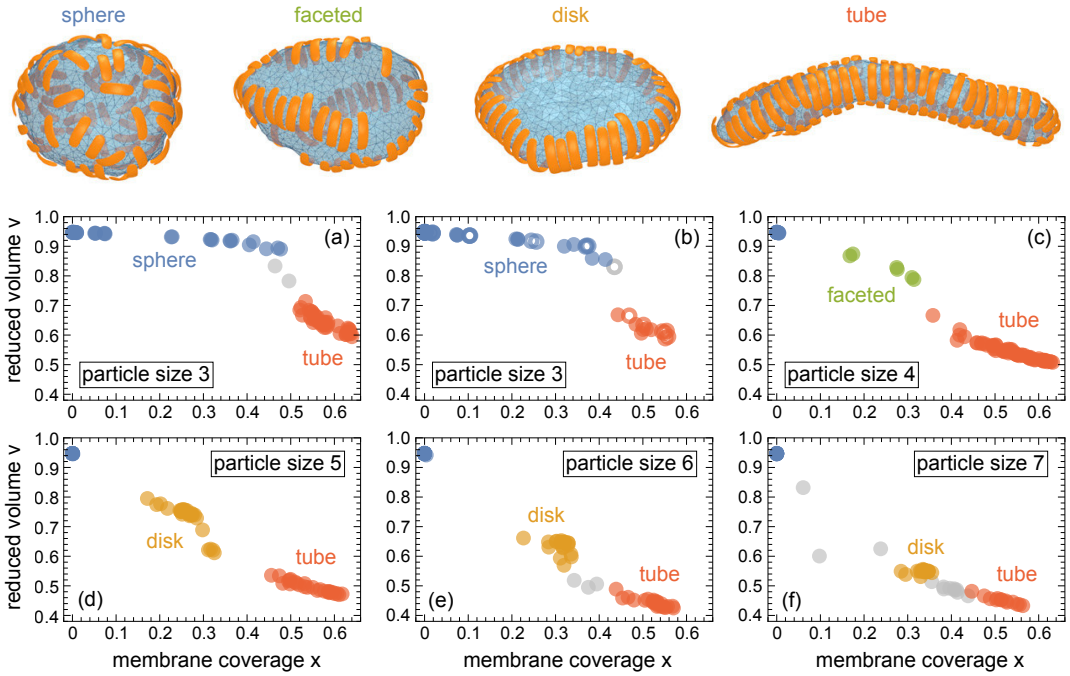

Figure 3.2.1.: These plots compare the membrane coverage and reduced volume for particles of specific size and θ_c. The colors represent different morphologies, with blue for spheres, red for tubules, orange for disks and green for faceted. Grey points are either intermediate or strongly metastable states. (a) displays particles of 3 segments with $\theta_c = 10°$ while (b) displays the same particles with $\theta_c = 3°$ (full circles) and $\theta_c = 5°$ (open circles). The remaining graphs (c), (d), (e), and (f) have $\theta_c = 10°$ and correspond to increasing particle sizes (4, 5, 6, 7). The gray points in (b) and (c) are partly tubular, while the grey points in (e) are disks connected to tubules. Finally, the grey points in (f) are partly formed tubules in a strong metastable state.

The tubular morphology appears at membrane coverage higher than 50% for $\theta_c = 10°$ or membrane coverage higher than 45% for $\theta_c = 3°, 5°$. Simulations with larger particles have all been carried out only with $\theta_c = 10°$. The tubular morphology appears at high membrane coverage for all particle sizes. Particles of four segments at low membrane coverage display a region where the membrane still resembles a distorted sphere, with particle lines and flattened regions, which is here denoted as *faceted* morphology. For particles of 5, 6, 7 segments the disk-like configuration of the membrane appears as an intermediate between tubular and spherical configurations for membrane coverages lower than 45%, while tubular configurations appear at higher concentrations. Particles of size 5 display a markedly more separated gap between the disk-like and tubular regions. Tubular structures with particles of size 5 are indeed surrounded by three lines of particles, which makes the transition to disk non-continuous. On the contrary, for particles with 6 and 7 segments, the tubular morphologies have two lines of bound particles, allowing a continuous transition between the disk-state and the tubule-state. Figure 3.2.2 shows the membrane morphologies in the graph of membrane coverage and mean induced angle by the particles. Small particles are able to bind at multiple locations independently of one another, whereas binding events are infrequent for larger particles. No binding events have been observed for particles of 7 segments if no other particles are already bound to the membrane.

Tubular morphologies have been observed for every kind of particle size at high area coverages. The radius of the tubule is related to the size of particles with smaller particles inducing thicker tubes, as shown in figure 3.2.3 and plotted in 3.2.9. There is an overall tendency of particles to be aligned side by side, which can also be observed in the temporal evolution of the system, especially in simulations starting from a sphere. Bound particles of size 3 do not display side-by-side alignments. On the contrary, larger particles form lines of particles. Specifically, four lines for particles of size 4, three lines for particles of size 5, and two lines for particles of size 6 and 7, see figure 3.2.4 for a schematic illustration. As there are no direct particle-particle interactions in the model (except for the hard-core repulsion), this ordering must be a result of membrane-mediated attractive interactions[59]. In previous research on similar topics, two kinds of alignments have been observed: the side-by-side one, as in this case, and the tip-to-tip one. The side-by-side alignment is compatible with the energy minimization conditions[41] or for membranes with high tensions[52]. The membranes in this project are tensionless. The tip-to-tip alignment has been observed in molecular dynamics simulations of N-BAR domains[51, 50] and it is likely to be caused by direct interactions between proteins ensuing from the molecular model. It is also relevant to note that multiple nucleation sites occur with smaller particles while for larger particles the binding happens primarily through membrane-mediation. The temporal evolution of the system starting from a sphere is illustrated in the examples in figures 3.2.5(a), 3.2.5(b), 3.2.5(c), whereas figure 3.2.6 shows the transformation of a disk into a tubule.

The disk is made of two flattened quasi-parallel or slightly-swollen sheets connected at their edges by a bent region, where the particles are bound. Disks have appeared

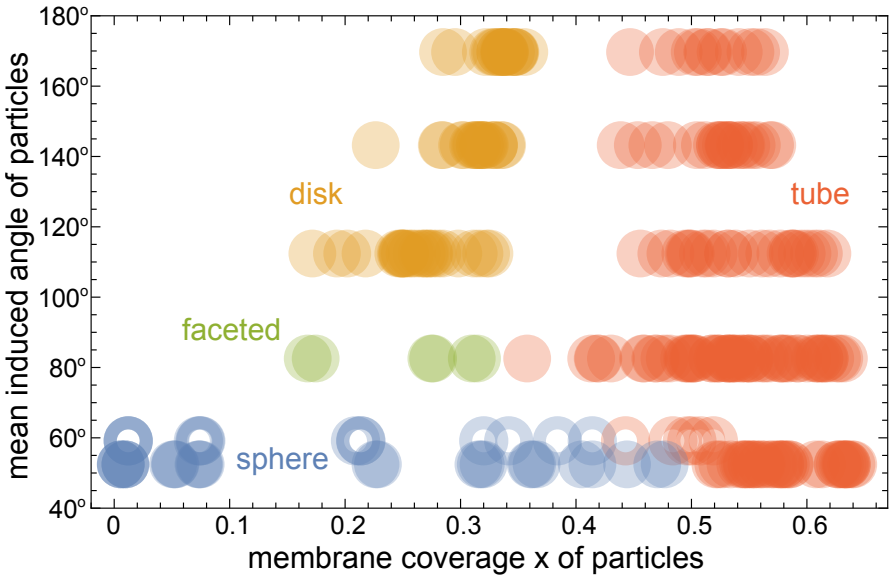

Figure 3.2.2.: Morphology diagram showing the mean induced angle versus the membrane coverage for the data points of figure 3.2.1. Open and solid circles represent simulation results with $\theta_c = 3°$ and $\theta_c = 10°$, respectively. The mean induced angle is the mean of the values of the angular distribution shown in figure 3.1.1. Colorings correspond to the morphology classification of the converged simulations.

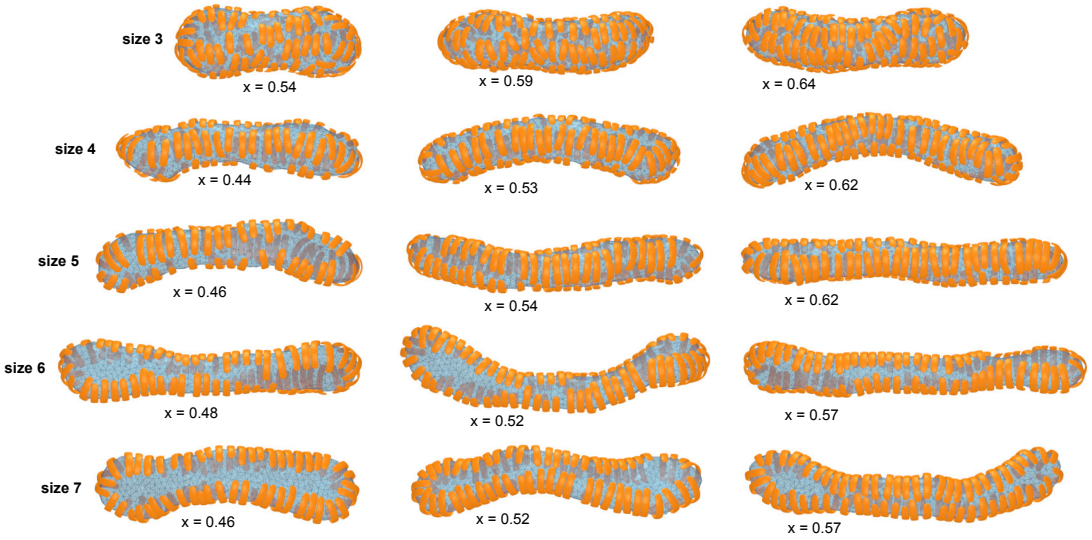

Figure 3.2.3.: Illustrations of exemplary morphologies of tubules of particles of size 3 to 7 with different membrane coverages x.

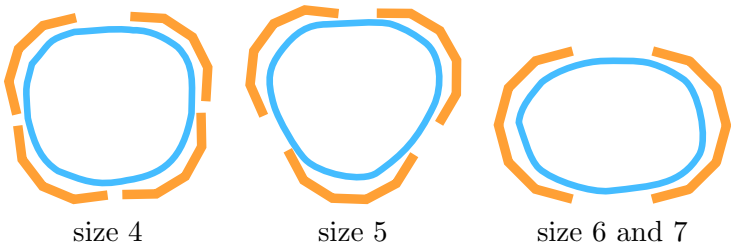

Figure 3.2.4.: Sectional scheme illustrating the lines arranged around tubules of particles with 4 to 7 segments. Particles of size 4 form four lines around tubules, while particles of size 5 the lines are three, and finally larger particles only form two lines.

with particles of 5, 6, 7 segments, with an intermediate amount of membrane coverage and a smaller thickness for larger particles, as illustrated in figure 3.2.7 and plotted in 3.2.9. These geometries are compatible with results from energy minimization[42]. It must be emphasized that unlike tubules, where the whole membrane area is a potential binding site, in disks only the edges have bound particles adsorbed to them. Therefore the membrane coverage by particles for disks is expected to scale like the square root $\sqrt{A}$ of the surface area A.

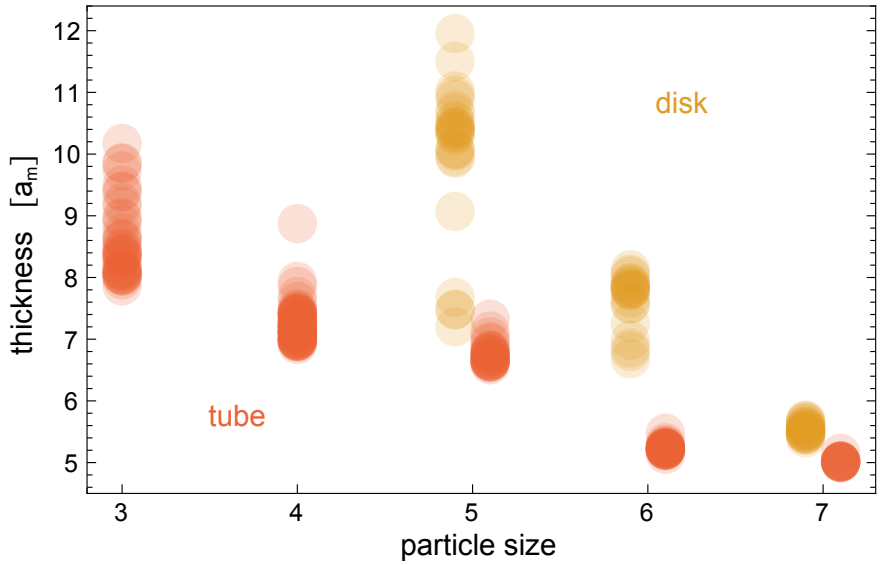

Figure 3.2.9.: Plot of the estimated tubule radius, as well as the disk thickness D_t at the center, measured in units of a_m and grouped by particle size. Both quantities decrease in magnitude with the particle size. This graph also shows that the ranges of both tubular radii and discoidal thicknesses are larger for smaller particles.

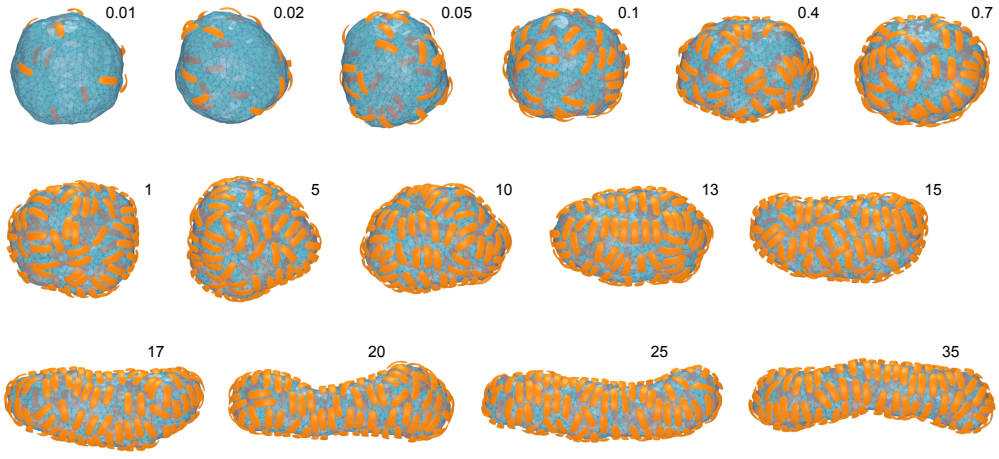

(a)

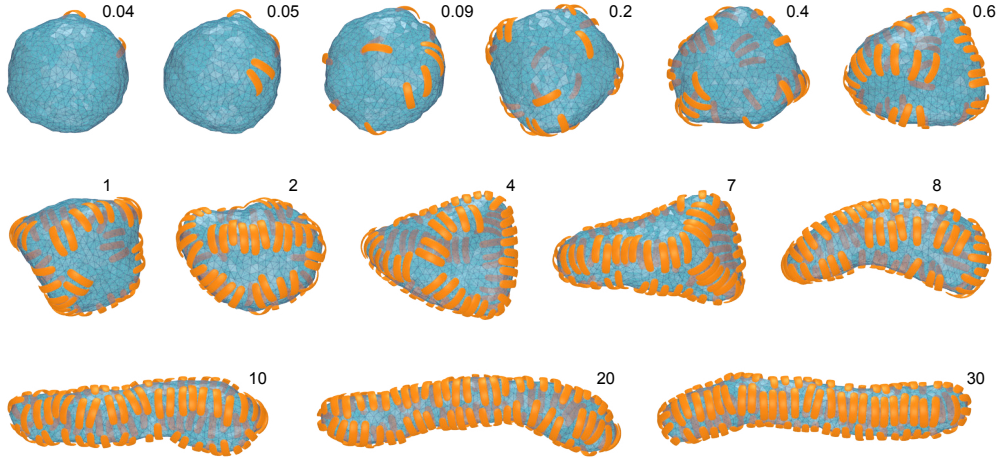

(b)

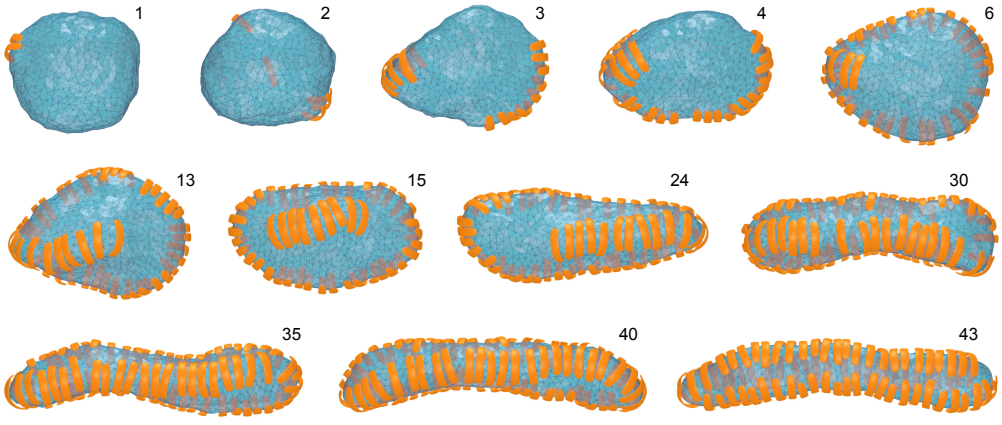

(c)

Figure 3.2.5.: Temporal morphological evolution starting from a spherical configuration and ending into a tubule. Units are 10^6 Monte Carlo steps per membrane vertex. Simulation with 400 particles. In 3.2.5(a) the particles have 3 segments and $U = 18k_BT$, in 3.2.5(b) the particles have 4 segments and $U = 18k_BT$, in 3.2.5(c) the particles have 5 segments and $U = 12k_BT$.

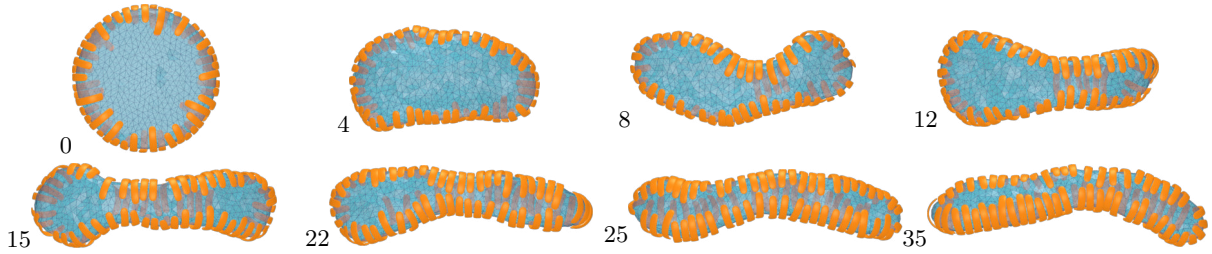

Figure 3.2.6.: Temporal morphological evolution starting from a discoidal configuration and ending into a tubule. Units are 10^6 Monte Carlo steps per membrane vertex. Simulation with 400 particles of size 5 and particle-membrane binding constant $U = 14k_BT$.

The computational results shown in this chapter can be compared with experimental results. In particular, the angle induced on the membrane by particles of 3 segments is compatible with the observed bendings caused by N-BAR domains such as Arfaptin, endophilin, and amphiphysin[38, 31]. In our model, the particles of 3 segments loosely surround the tubular morphologies, forming short-ranged arrangements only. This is compatible with electron tomography observations of the Bin1 N-BAR domain[11]. As follows, it is reasonable to hypothesize that Bin1 proteins lack of meaningful direct protein-protein interaction in Bin1 proteins[11], as the model presented in this project treats particle-particle interactions just as hard-core repulsions. The percentage of membrane covered by particles is in agreement with fluorescence experiments. For example, it has been determined that $\beta 2$ centaurin covers around $37 \pm 9\%$ of the membrane area, while endophilin covers $44 \pm 27\%$ of tubules pulled with optical tweezers from membrane vesicles[49].

In previous computational models for the interaction of arc-shaped particles and biological membranes the particles were embedded in the membrane, as they could not unbind. Tubular structures and disk-like sheets have already been observed with elastic membrane models[2, 3, 39, 55, 35, 36]. Models treating curvature-inducing particles as embedded elements of the membrane have been proposed. For example, a recent model treats the particles as nematic objects on the vertices of a triangulated membrane[39, 55], while another treats them as sequences of beads embedded in a membrane represented by a two-dimensional sheet of beads[35, 36]. These models, having a fixed number of particles on the membrane in a canonical ensemble, lead to aggregation areas of particles where a strong membrane curvature is induced, while many regions with low particle concentrations and weak membrane curvature persists.

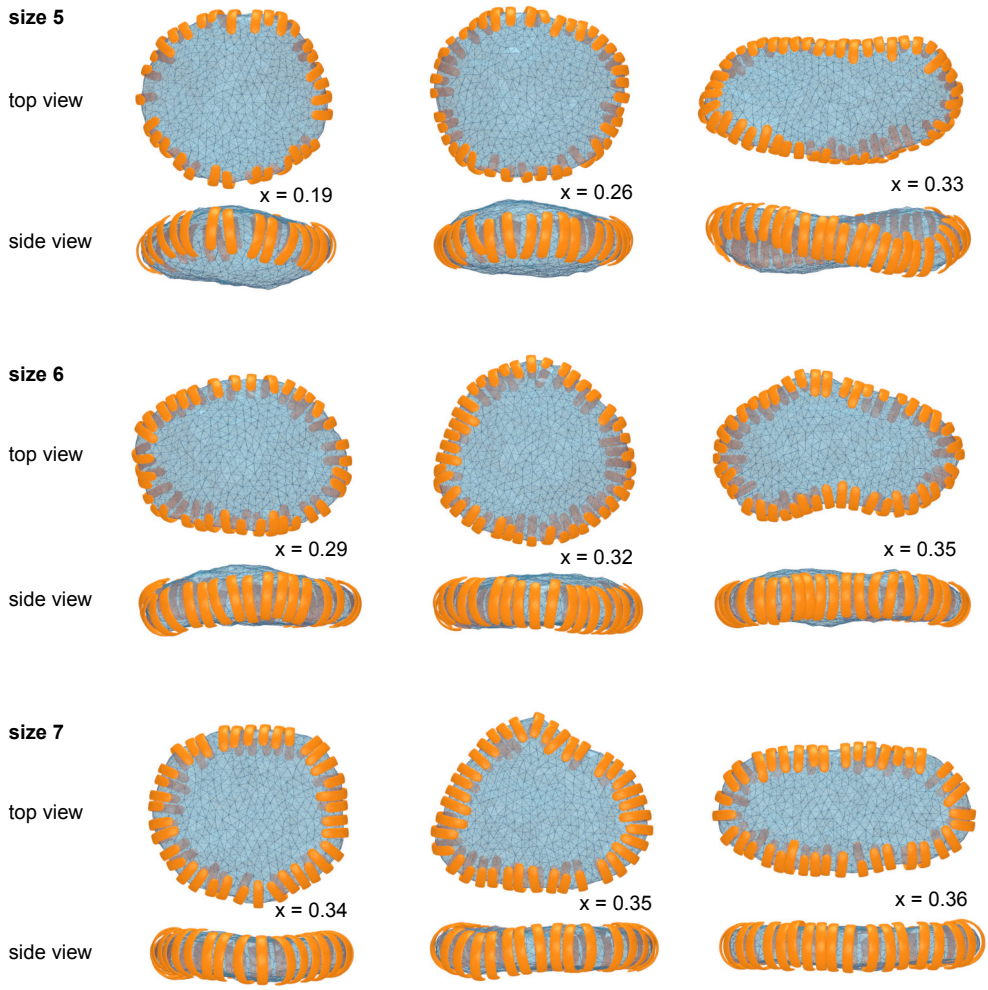

Figure 3.2.7.: Examples of system states in discoidal morphologies. The rows categorize the particles of 5, 6, 7 segments while the variable x is the membrane coverage ratio.

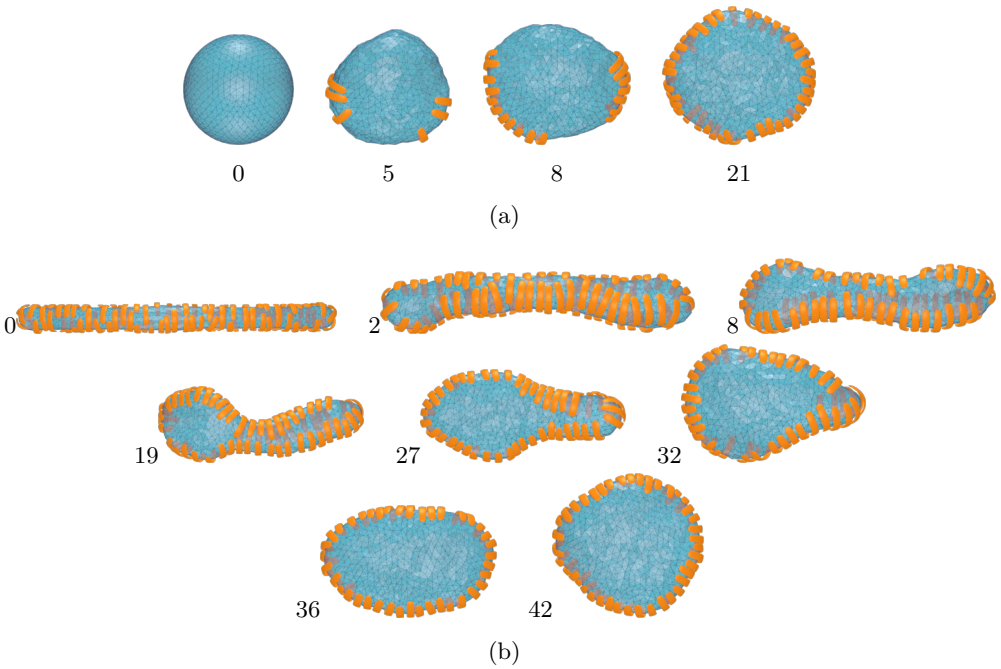

Figure 3.2.8.: Formation of the disk morphology in a sytem with $N = 400$ particles. Time is in 10^6 Monte Carlo steps per vertex units. In 3.2.8(a) the particles have 5 segments and $U = 10k_BT$. Two nucleation sites are visible, two lines of particles are then formed, which end up merging forming the edge of the disk. Starting from a tubule in 3.2.8(b), with particles of size 5 and $U = 8k_BT$.

4. Shaping of membranes by mixtures of concave and convex particles

Mixtures of concave and convex particles can be expected to generate membrane morphologies with regions of negative curvature. One of the motivations for the introduction of a second type of particles, the is convex ones, is the suggestion that three-way junctions are stabilized by such particles[9, 8, 40]. Three-way junctions are interconnections of three membrane tubules occurring in the endoplasmic reticulum. They are mostly present in the peripheral ER and are highly dynamic, continuously undergoing transformations. The Lunapark protein (Lnp1) has been shown to stabilize the formation of three-way junctions[9, 8, 40]. Experimental evidence suggests that this molecule is composed of two transmembrane domains, possibly forming an arc-like shape, which may resemble the BAR-domain or reticulon molecules that have been investigated in chapter 3, with the difference that the Lnp1 is expected to bind to the membrane on its convex side, therefore inducing negative curvature or invaginations on the membrane[8]. The three-way junction may be illustrated as the junction of three tubular legs converging to an intersection point, see figure 4.0.1. At the junction, the three pairwise connections between tubules include saddle-like regions of the surface, having directions with both positive and negative curvatures. In this chapter, convex particles, which mimic the proposed shape of Lnp1, are added to the system and the membrane morphologies are investigated for different relative concentrations of particle types.

In our model, both concave or convex particles interact with the same adhesion energy U per particle segment. Therefore, the relative membrane coverage of the two types is primarily regulated by the overall particle concentrations. The adhesion energy ranges

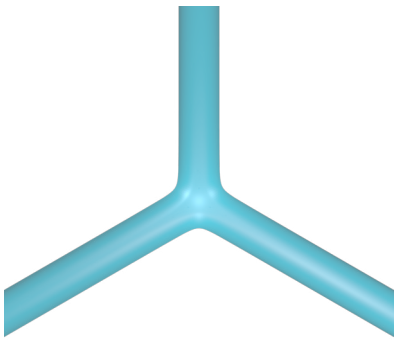

Figure 4.0.1.: Illustration of an ideal three-way junction connecting three tubules.

in the $U = 7, \ldots, 14$ interval. In this chapter, a larger triangulated membrane has been used, with $n_T = 5120$ triangles. The larger size is motivated by a greater area required by the three-way junction morphology. The angular threshold for equation 2.1.13 is always kept at $\theta_c = 10°$ in all simulations. Ensembles of mixtures of the two types of particles are considered, with N_1 concave- and N_2 convex-interacting number of particles. The concentration of convex-interacting particles relative to the total number of particles is defined as

$$d_{\text{convex}} = \frac{N_2}{N_1 + N_2}.$$

Concentrations of varying amounts of convex-interacting particles have been used, namely $d_{\text{convex}} = 0.0$, 0.02, 0.05, 0.1, 0.2, 0.4, and 1.0. Particles of the same type have the same number of segments, but the sizes of particles for the two different types may be different. The combinations (s_1, s_2) of particle sizes used in the simulations are $(3, 3)$, $(4, 3)$, $(4, 4)$, $(5, 3)$ and $(5, 5)$. The total number of particles in the system is held constant at $N_1 + N_2 = N = 400$, which is enough to guarantee a reservoir of unbound particles. Low concentrations of concave-interacting particles are the primary focus. In the simulations, the initial morphologies for the membrane are the sphere, the tubule, and disks with the addition of a three-way junction. The initial morphologies of tubule, disk, and three-way junction are stabilized by particles that are already bound at the start of the simulation, see section 2.2.1. In this chapter, the volume V of the space enclosed by the membrane is allowed to freely fluctuate. Therefore, the constant c_V in equation 2.1.8 has the value 0. Additionally, the bending rigidity of the membrane is $\kappa = 10 k_B T$ for all simulations.

4.1. Membrane-mediated segregation and bulged balls

Particles of the same type tend to form lines through membrane-mediated interactions. Segregation of particles by type is also observed, whereby side-by-side alignments of concave particles form elongated bulges while side-by-side alignments of convex particles form invaginations resembling valleys. At high coverages of convex particles, the membrane looks like a bulged ball, with many valleys of invaginations separated by lines of bulges, see figure 4.1.1(a) and (b). In some cases, double lines of the same particle type are also observed, see the first, third and fourth figures in 4.1.1(b). In this configuration, the prevalent adsorbed particle type appears to form a connected region of aligned particles on the membrane, while the other type of particles aggregate in disconnected clusters.

Particles of 3 segments form moderate bulges on the membrane, and their side-by-side alignments appear quite irregular, especially for the concave particles, see figure 4.1.1a. For particles with 4 or 5 segments, the protrusions are more pronounced and the side-by-side alignments are straighter, see figures 4.1.1(b) and 4.1.1(c).

The dynamical formation of the bulged ball with particle segregation is straightforward for all particle sizes. Figure 4.1.2(a) illustrates the temporal evolution of a sphere into a bulged ball with particles of size 3 where the ratio of convex to total particles is $d_{\text{convex}} = 0.2$, resulting in a prevalence of concave particles covering the membrane. Concave

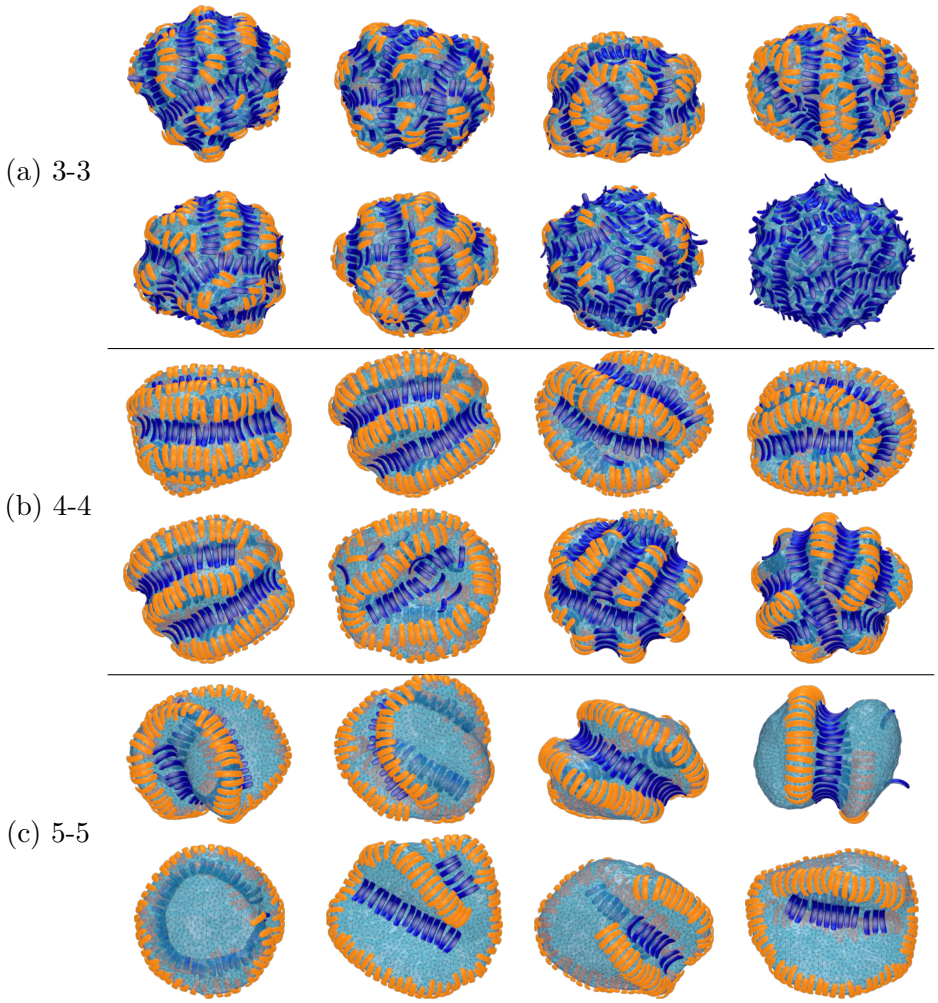

Figure 4.1.1.: Exemplary morphologies in which the membrane is covered by both concave and convex particles. Membranes covered by a significant amount of convex-interacting particles resemble bulged balls. Convex particles (blue) induce invaginations while concave particles (orange) fill the hilly bulges. The protrusions are less marked for smaller particle sizes. Group (a) shows examples of morphologies of membranes covered by particles of 3 segments. Group (b) shows membranes with particles of 4 segments and deeper valleys. Group (c) displays membranes with particles of size 5, where the bulging is extremely marked and entire regions of the membrane are not covered with particles at all. All figures display segregation of concave and convex particles, arising from membrane-mediated interactions.

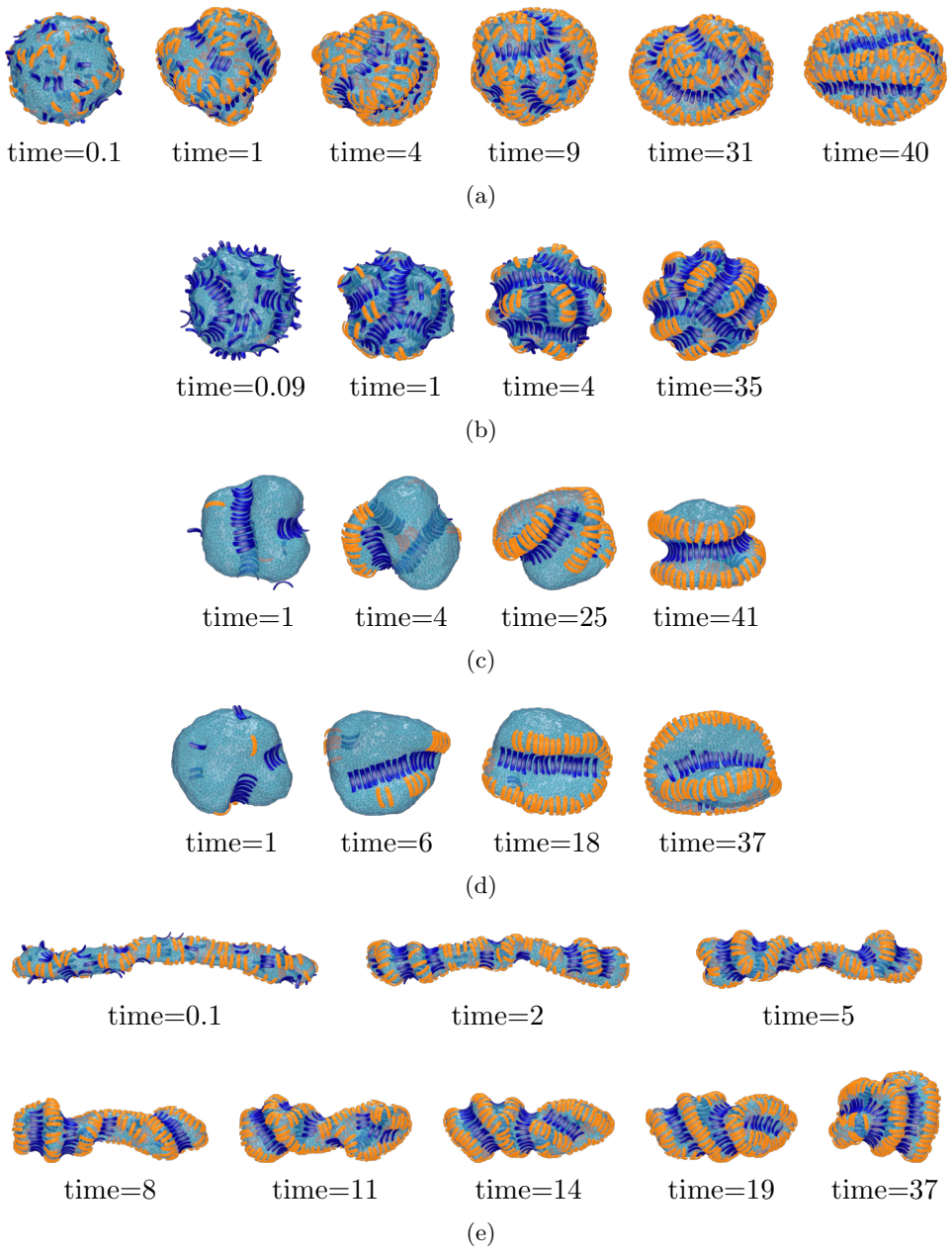

Figure 4.1.2.: Exemplary time sequences of simulations with morphological change to bulged ball. Time is expressed in 10^6 MC steps per vertex. The starting morphology of the membrane for this simulation is a sphere. The adhesion energy are $U = 11\,k_BT$ for (a), $U = 12\,k_BT$ for (b), $U = 9\,k_BT$ for (c), $U = 13\,k_BT$ for (d), and $U = 11\,k_BT$ for (e). The concentrations of convex particles are $d_{\text{convex}} = 0.2,\ 0.4,\ 0.1,\ 0.05,\ 0.2$ respectively. The sizes of concave-convex particles are $(3,3)$, $(4,4)$, $(5,5)$, $(5,5)$, and $(4,4)$ respectively. (a), (b), (c), (d) start from an initial sphere whereas (e) starts from a tubule.

particles form therefore a connected region isolating some clusters of disconnected convex lines. A sample for the temporal evolution of particles of size 4 (both concave and convex) is shown in figure 4.1.2(b), where the concentration of convex to total particles is $d_{\text{convex}} = 0.4$. The larger size of the particles produces higher bulges, and the relatively high coverage of convex particles creates isolated clusters of concave particle alignments. Figures 4.1.2(c) and 4.1.2(d) illustrate the temporal evolution of a sphere into a bulged ball with particles of 5 segments. In this case, the bulgings are extremely marked and the membrane coverage is lower. The larger induced curvature, presumably, does not allow alignments of particles of different types close to each other. Note that the bulged ball morphology appears to be common at high concentrations of convex particles and is probably independent of the initial shape. For example, figure 4.1.2(e) shows the temporal evolution of a tubule into a bulged ball for particles of size 4 and $d_{\text{convex}} = 0.2$.

4.2. Converged morphologies

Mixtures of concave and convex particles with 3 segments induce various morphologies depending on the relative coverage of convex and concave particles d_{convex} as well as the total membrane coverage. Figure 4.2.1 shows a sequence of converged membrane morphologies of simulations starting from a sphere with particles of size 3 ordered by increasing reduced volume. The vesicles with low reduced volume ($v < 0.55$) exhibit tubules, have a high membrane coverage ratio and are predominantly covered by concave particles. Isolated clusters of convex particles are present. In some cases the tubules are marked by sharp bends, which turn the membrane into a U shape. Small clusters of convex particles are located on the inner side of the curve, suggesting that convex particles are responsible for the production of U-shaped tubules. At intermediate values of the reduced volume of the membrane $v \approx 0.55 - 0.90$, the bulged ball is the primary morphology. The membrane coverage is high and two different kinds of bulged balls are distinguishable, depending on the relative concentration of concave and convex particles. At higher values for the reduced volume, i.e. $v > 0.90$, lower membrane coverages are observed. Both concave and convex particles appear to be loosely distributed around the ball.

Figure 4.2.2 shows examples of membranes for simulations starting from a sphere with particles of size 4 ordered by increasing values of their reduced volume. Mixtures of particles with 4 segments at low reduced volume ($v < 0.55$) are predominantly covered by concave particles, they produce tubular morphologies or three-way junctions. Convex particles along tubules may form isolated clusters of lines following the tubular orientation. Three-way junctions are completely covered with concave particles except for one of the three saddle regions at the junction, which presents a short line of convex particles. It may be assumed that such a cluster acts as an anomaly generating a third leg out of the tubule, thus inducing the morphology of a three-way junction. At middle values for the reduced volume ($0.55 < v < 0.8$), the bulged ball occurs again, the membrane coverage is still high but wth various concentrations of convex particles. If the concentration of concave particles is not low, the bulged ball presents extremely

marked curvatures of valleys and outward bulgings. At high values for the reduced volume ($v > 0.8$), the membrane coverage by particles is very low and the membrane is in a spherical morphology.

Figure 4.3.7 compares exemplary U-shaped membranes for particles of size $(3, 3)$, $(4, 3)$, and $(4, 4)$. Figures 4.3.8, 4.3.9, and 4.3.10 illustrate examples of formation of U-shaped membrane morphologies.

4.3. Stability of three-way junctions

Converged three-way junction morphologies can be observed in two kinds of simulations: (1) simulations starting from an initial configuration other than the three-way junction and (2) simulations starting from the three-way junction.

Formation of three-way junctions The formation of three-way junctions from a sphere was observed only with particles of size 4. Figures 4.3.1 and 4.3.11 illustrate examples of the formation of three-way junctions from a spherical morphology. A small cluster of convex particles appears to be disrupting the formation of a tubular structure induced by the concave particles. This allows a third leg to jut out of the sphere, which is then extended by the adsorption of concave particles. The small line of convex particles remains bound to one or two of the three saddle regions of the junction.

Simulations starting from three-way junctions In order to investigate the stability of three-way junctions, further simulations have been run with the three-way junction as initial shape for combinations of sizes of concave and convex particles (s_1, s_2) is $(3, 3)$, $(4, 3)$, $(4, 4)$, and $(5, 3)$. Systems with both concave and convex particles of size 3 are illustrated in figure 4.3.2. The three-way junction morphology has been preserved at low coverage of convex particles and in some cases, surprisingly, even without adsorbed convex particles. At high membrane coverages, a higher concentration of convex particles among the adsorbed particles results in the structure breaking up and turning into an elongated ball with clustered groups of convex particles. Some of the membranes have turned into a U-shaped tubule, thus losing one of the three legs.

For simulations with concave particles of size 4 and convex particles of size 3, the morphologies stabilized into a three-way junction have their saddle regions covered with concave particles, unlike other cases, see figure 4.3.3. The convex particles tend to cluster on the sides of the three-way junction. Double lines of concave particles aligned side-by-side cover the three saddles of the junction, which are extensions of the four lines surrounding the tubular morphologies with particles of size 4. For larger amounts of convex particles, the three-way junction structure is disrupted and turns into a tubule with invaginations.

When both concave and convex particles have size 4, the locations of the saddles of the junction show a competition between coverings by double lines of concave particles connecting two tubular legs, and short lines of side-by-side aligned convex particles, see figure 4.3.4. Higher amounts of convex particles appear to disrupt the junction.

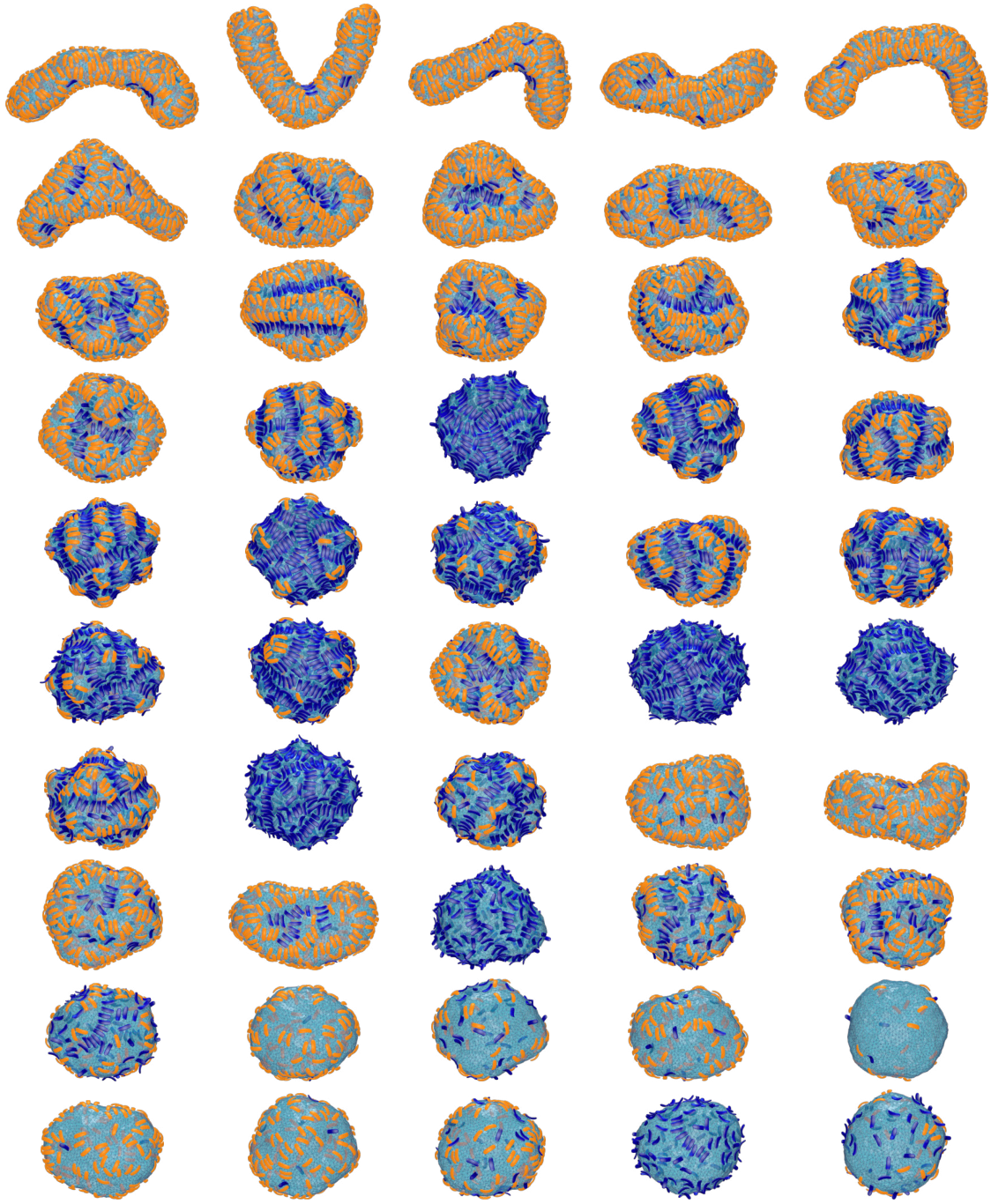

Figure 4.2.1.: Converged morphologies with mixtures of particles of size 3 ordered by the reduced volume of the enclosed space. All these samples have started from an initial spherical membrane morphology. Ordinary and U-shaped tubules are seen on the first line, at higher reduced volume the membrane turns into a bulged ball and then into a sphere.

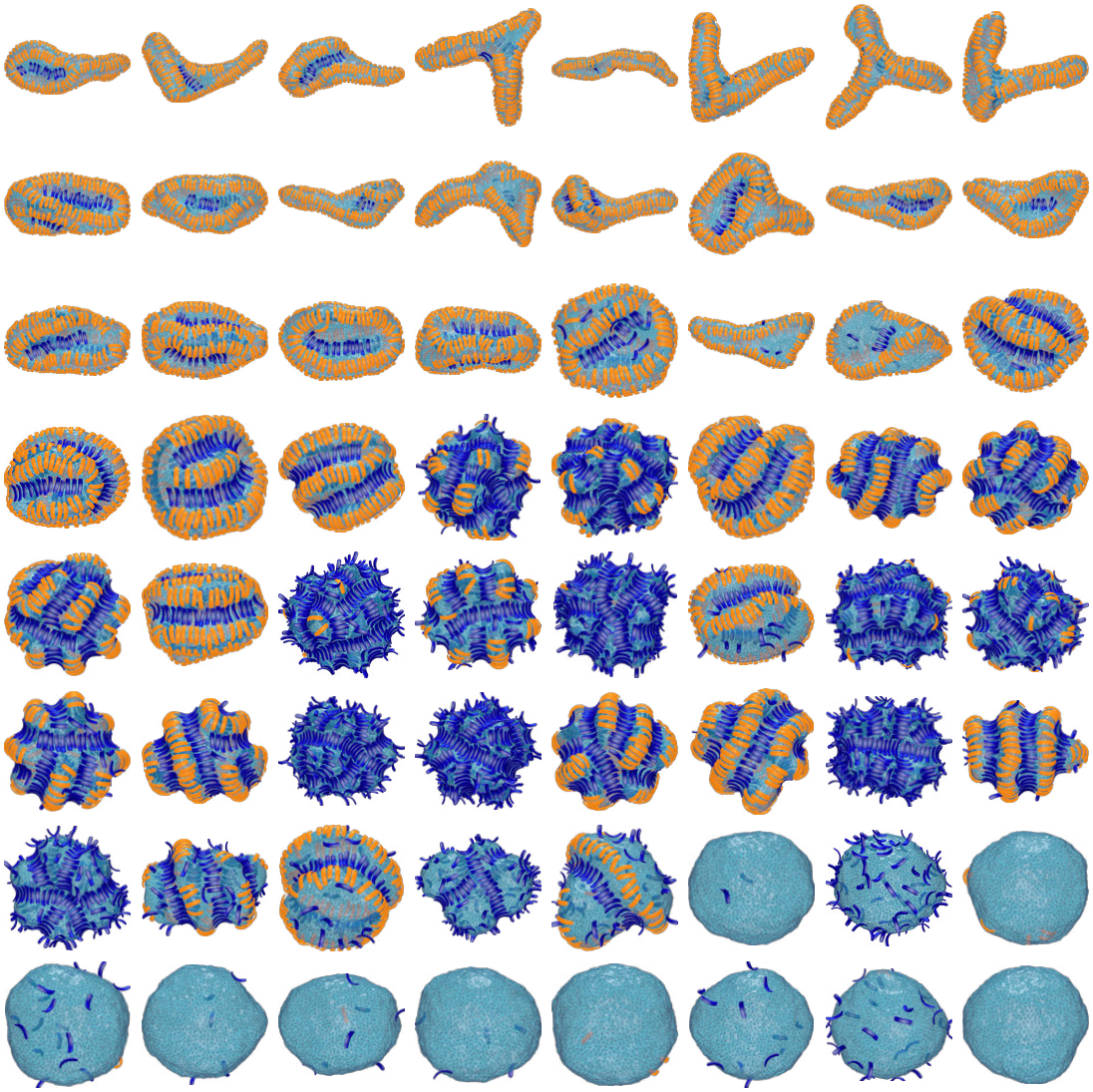

Figure 4.2.2.: Converged morphologies resulting from simulations with initial spherical morphology with mixtures of particles of size 4 ordered by the reduced volume of the enclosed space. Tubules and three-way junctions are spotted at low reduced volume, while the bulged balls appear at higher concentrations of adsorbed convex particles.

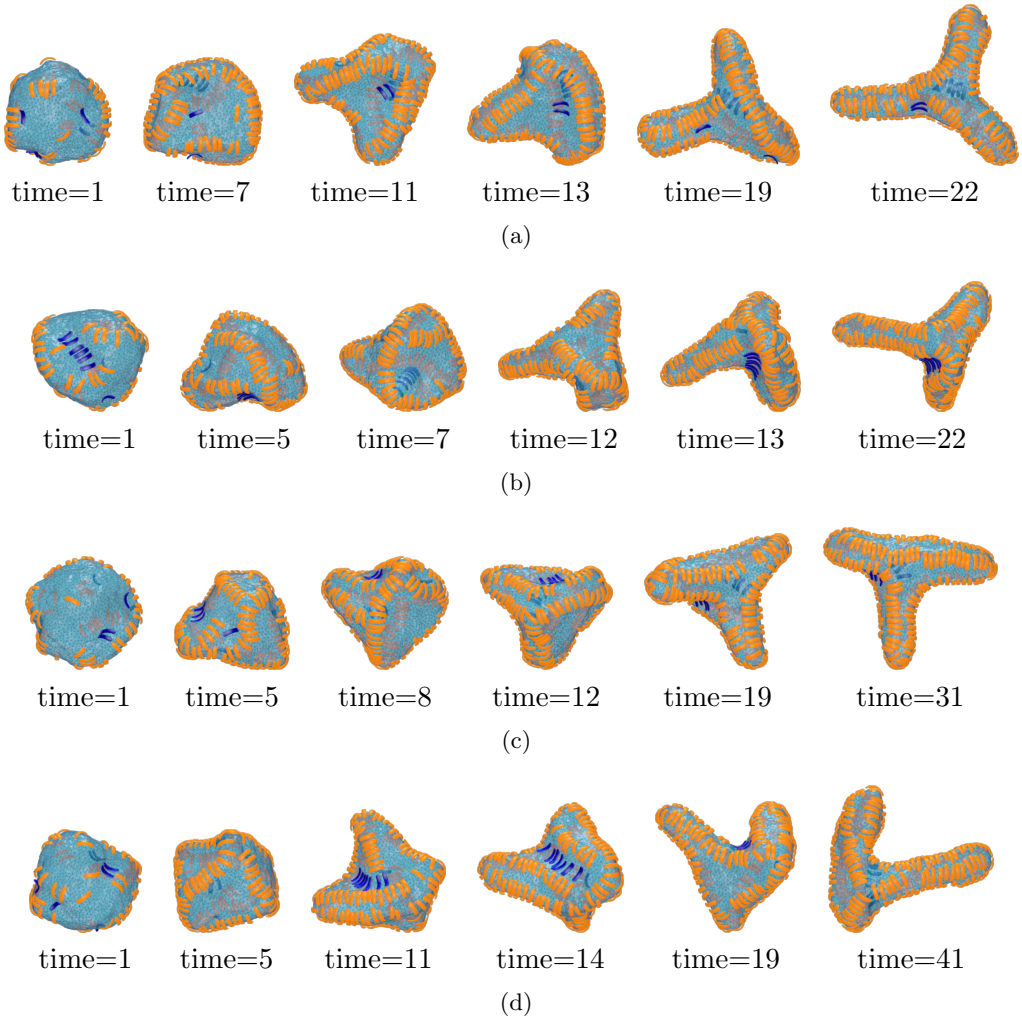

Figure 4.3.1.: Exemplary time sequences of morphological changes from spheres to three-way junctions. Time is expressed in 10^6 MC steps per vertex. The concentration of convex-interacting particles is 0.02. Both the concave-interacting particles and the convex-interacting particles have 4 segments. The starting morphology of the membrane for this simulation is a sphere. The adhesion energy in 4.3.1(a) is $U = 10\,k_BT$, in 4.3.1(b) is $U = 11\,k_BT$, in 4.3.1(c) is $U = 12\,k_BT$ and in 4.3.1(d) is $U = 14\,k_BT$.

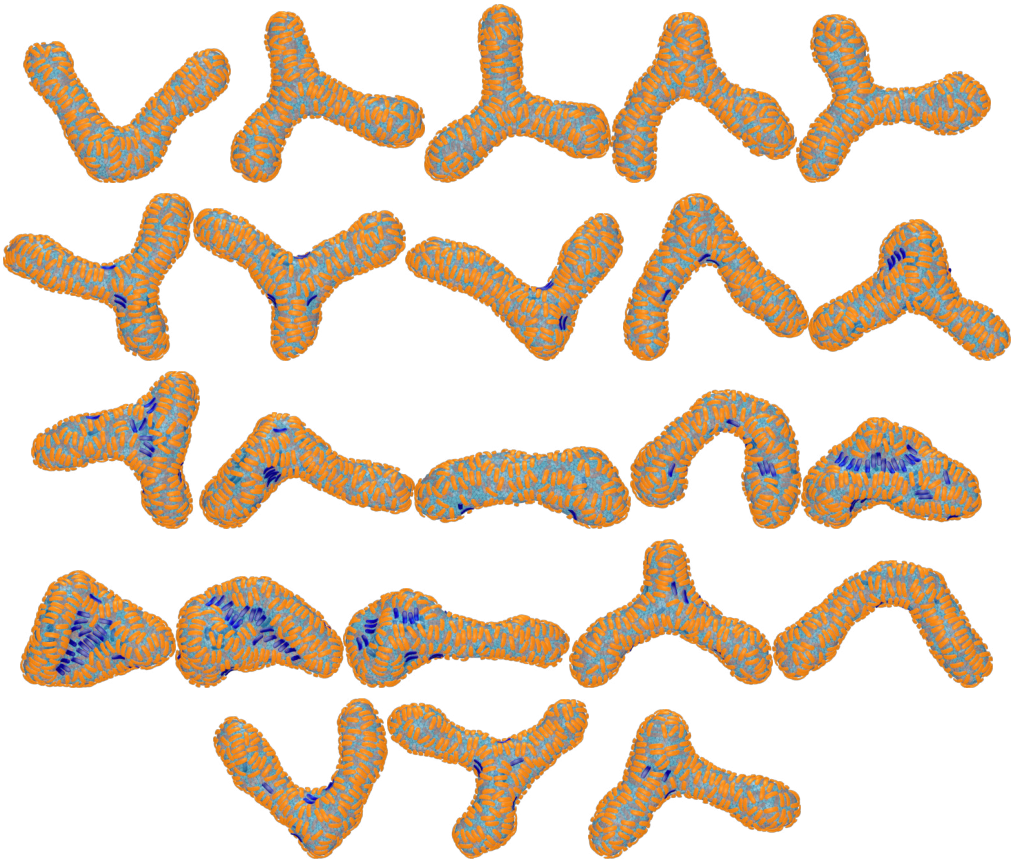

Figure 4.3.2.: Morphologies resulting from simulations starting as three-way junctions, with particles of size 3. Low concentrations of convex particles appear to stabilize the three-way junction structure, while higher concentrations disrupt the structure into an elongated tubule.

Mixtures of particles with concave size 5 and convex size 3 always show the transition from the three-way junction to either disks or faceted shapes with three lines of concave particles, with convex particles loosely bound to isolated locations of the membrane, see figure 4.3.5. It appears that three-way junctions are unstable states for these combination of particle sizes.

Figure 4.3.6 compares examples of three-way junctions for combinations of particles with (s_1, s_2) of $(3, 3)$, $(4, 3)$, and $(4, 4)$. The reduced volume for the membrane ranges from 0.43 to 0.55.

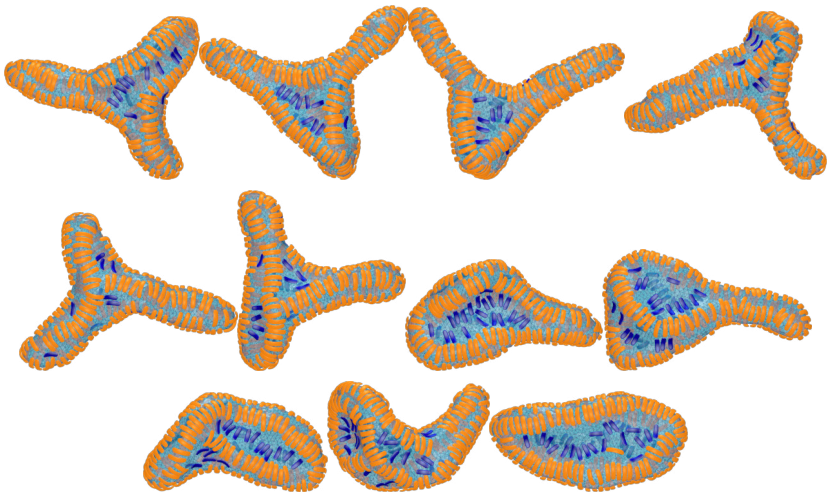

Figure 4.3.3.: Examples of simulations starting as three-way junctions with concave particles of size 4 and convex particles of size 3. Concave particles of size 4 are able to control the saddle-like regions of the junction, while convex particles are loosely clustered on relatively flat regions.

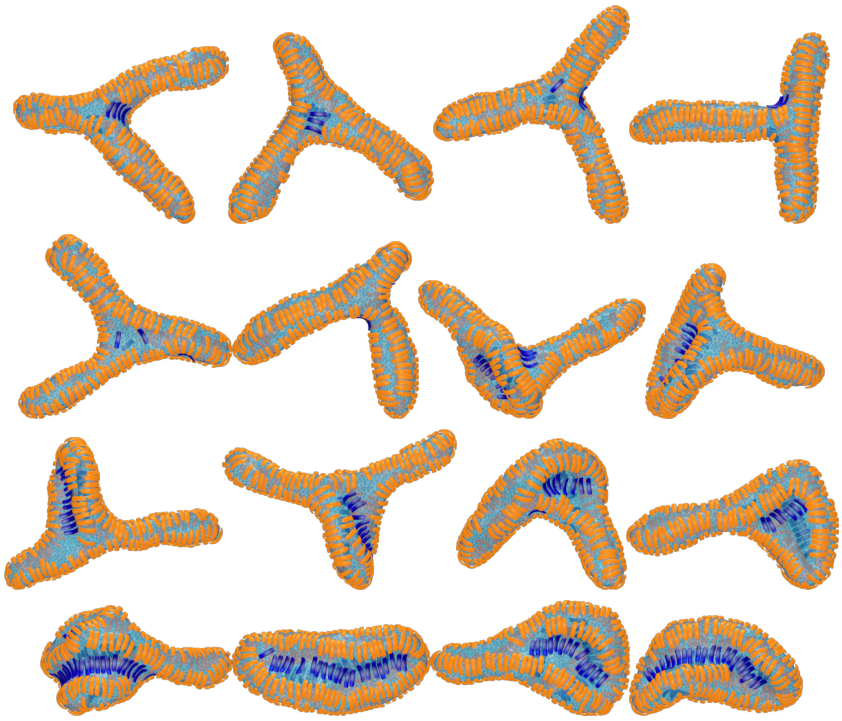

Figure 4.3.4.: Examples of morphologies from simulations starting as three-way junctions with particles of size 4. Convex particles tend to form short lines on one saddle region of the junction. Higher amounts of adsorbed convex particles disrupt the structure of the junction.

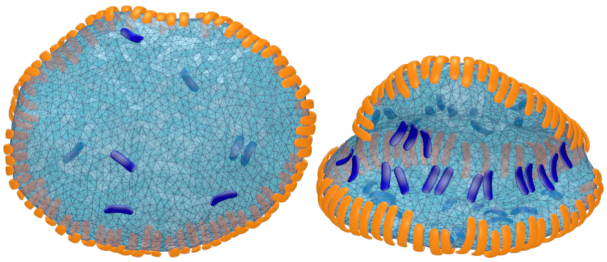

Figure 4.3.5.: Examples of two simulations starting as three-way junctions with concave particles of size 5 and convex particles of size 3. The initial morphology is not preserved, as the membrane is transformed into either a disk or a folded disk, as shown in the pictures.

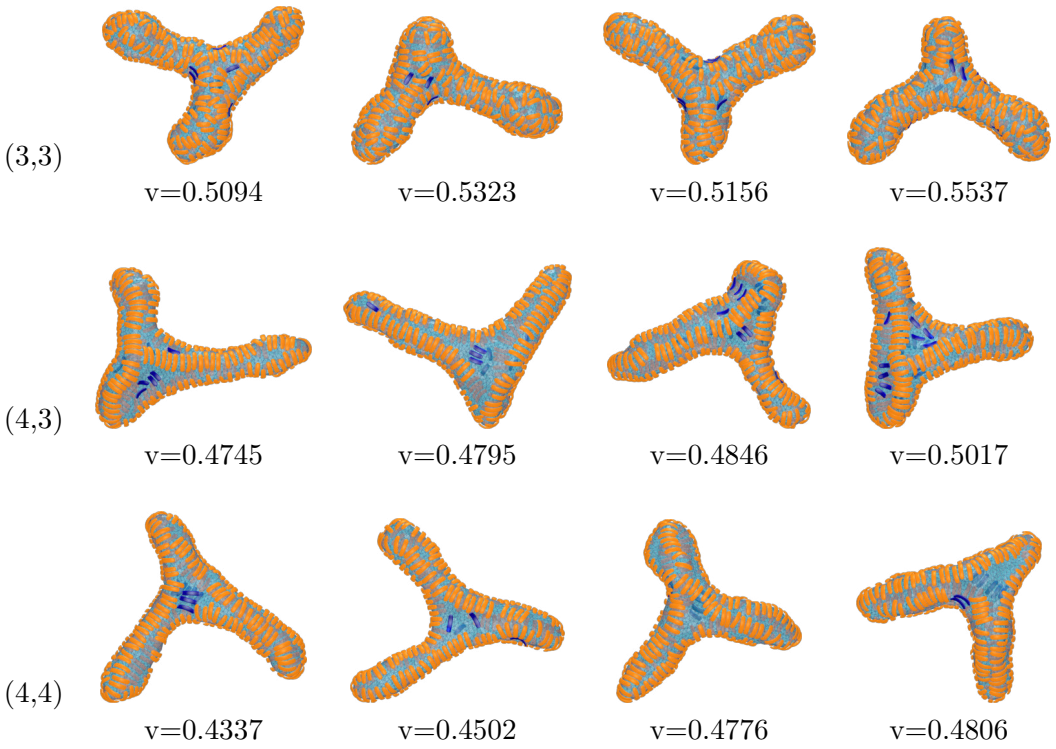

Figure 4.3.6.: Examples of three-way junction morphologies for different particle sizes. The reduced volume of the membranes is reported. Sizes for particle types of $(3,3)$, $(4,3)$, and $(4,4)$ are shown. Convex particles (blue) are located near the junction while concave particles (orange) cover all sides.

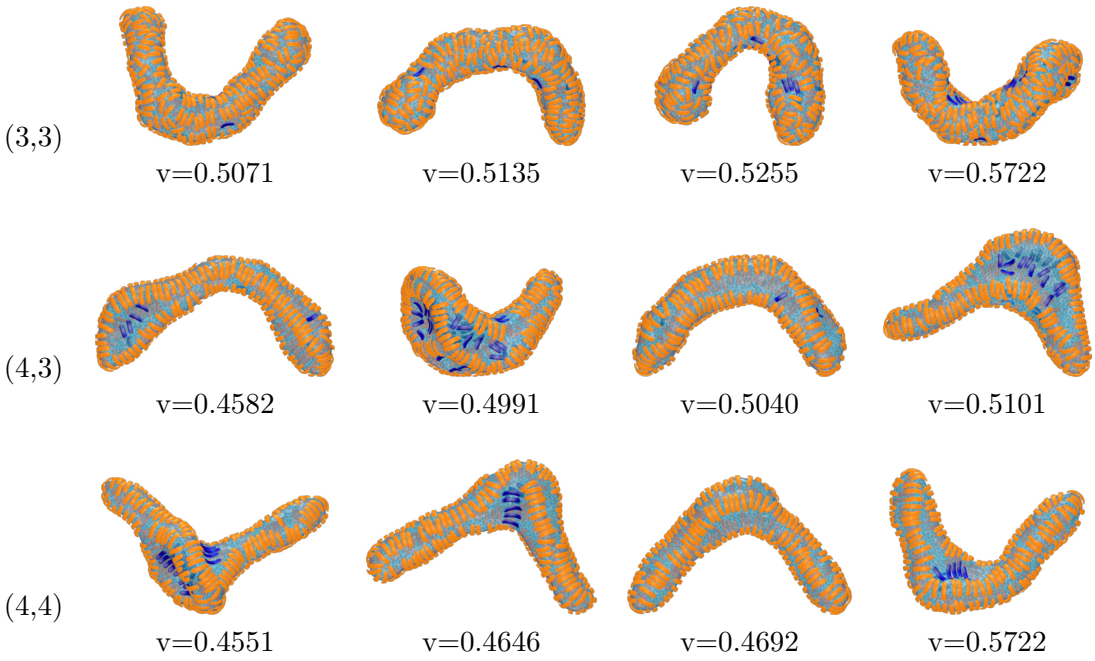

Figure 4.3.7.: Examples of U-shaped tubule morphologies. The reduced volume of the luminal space of the membranes is reported. Particle types of size $(3, 3)$, $(4, 3)$, and $(4, 4)$ are shown. Convex particles (blue) are often located on the saddles of tubular bends while concave particles (orange) cover the whole membrane.

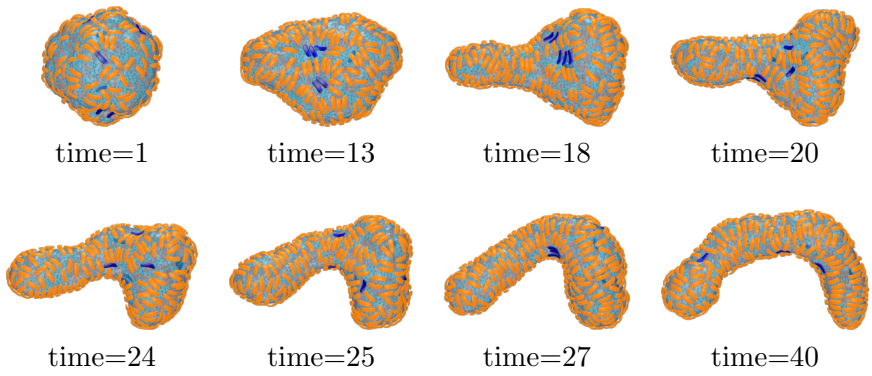

Figure 4.3.8.: Exemplary time sequence of a morphological change from sphere to U-shaped tubule. Time is expressed in 10^6 MC steps per vertex. In this simulation, the adhesion energy is $U = 13\ k_BT$. The concentration of convex-interacting particles is 0.02. Both the concave-interacting particles and the convex-interacting particles have 3 segments. The starting morphology of the membrane for this simulation is a sphere.

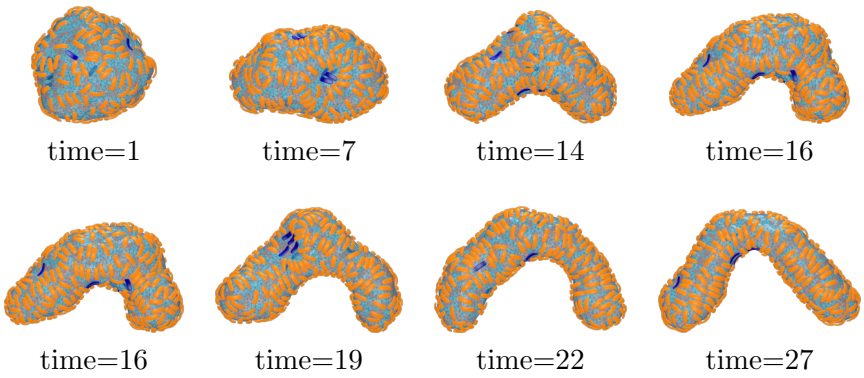

Figure 4.3.9.: Exemplary time sequence of a morphological change from sphere to U-shaped tubule. Time is expressed in 10^6 MC steps per vertex. In this simulation, the adhesion energy is $U = 9\ k_BT$. The concentration of convex-interacting particles is 0.02. Both the concave-interacting particles and the convex-interacting particles have 3 segments. The starting morphology of the membrane for this simulation is a sphere.

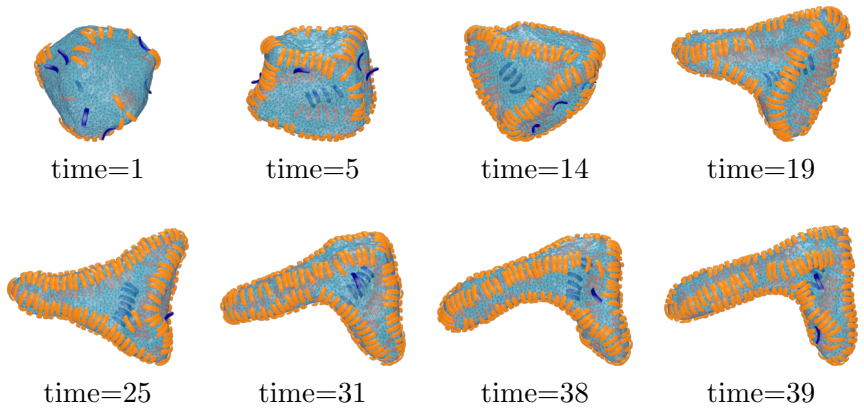

Figure 4.3.10.: Exemplary time sequence of a morphological change from sphere to U-shaped tubule. Time is expressed in 10^6 MC steps per vertex. In this simulation, the adhesion energy is $U = 8\ k_BT$. The concentration of convex-interacting particles is 0.02. Both the concave-interacting particles and the convex-interacting particles have 4 segments. The starting morphology of the membrane for this simulation is a sphere.

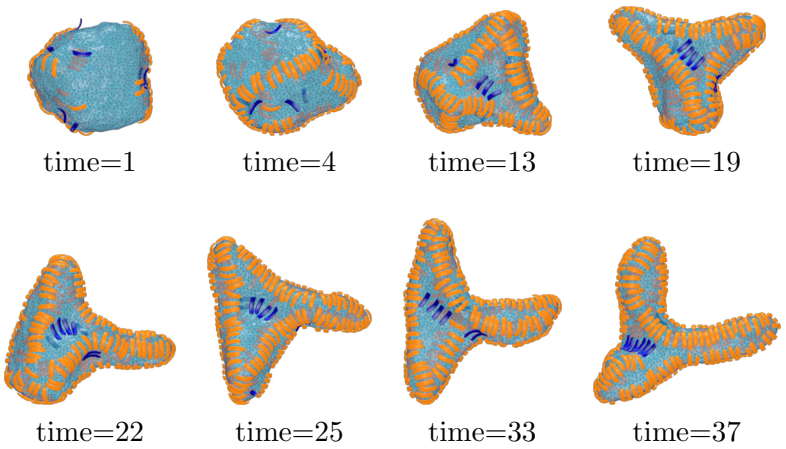

Figure 4.3.11.: Time sequence of a morphological change from sphere to three-way junction. Time is expressed in 10^6 MC steps per vertex. In this simulation, the adhesion energy is $U = 9\ k_BT$. The concentration of convex-interacting particles is 0.02. Both the concave-interacting particles and the convex-interacting particles have 4 segments. The starting morphology of the membrane for this simulation is a sphere.

5. Membrane-mediated interactions between particles

The adsorption of arc-like particles to the membrane leads to membrane-mediated interactions between membrane-bound particles[59]. These indirect, membrane-mediated interactions arise because the membrane curvature induced by the arc-like particles costs bending energy[59]. This cost depends on the distance and relative orientation of the particles and has been shown to result in a strong attraction between concave arc-like particles if the particles are oriented side-by-side[41, 59].

In statistical mechanics, the free energy of the interaction between two particles in a complex system may be deduced from the radial distribution function $g(r)$, which describes the density variation in number of particles with respect to the distance r from a reference particle. The complete interaction energy between particles may be computed from the radial distribution function $g(r)$ of particle pairs and its link to the particle-particle interaction energy $w(r)$ provided by the reversible work theorem[7]

$$g(r) = \exp\left(-\frac{w(r)}{k_B T}\right) \tag{5.0.1}$$

where r is the distance between two particles, k_B is the Boltzmann constant, and T is the temperature of the system. The interaction between particles of 3 and 4 segments adsorbed to tubules and spheres is studied and quantified in this chapter. The triangulated membrane with $n_T = 2000$ triangles has been employed. The simulation runs in a box with periodic boundary conditions and volume $V_{\text{box}} \approx 3 \cdot 10^5 a_m^3$. This is 64 times as large as the volume of a perfect sphere, slightly larger than the size of the box described in equation 2.2.1.

Previous investigations of the membrane-mediated interaction between particles bound to a membrane have largely focused on planar morphologies[**?**]. Only recently, membrane-mediated interactions between Janus particles adsorbed to curved morphologies have been investigated[**?**]. Here, in order to investigate the membrane-mediated interaction of concave particles bound to a curved membrane, a further constraint on the enclosed volume of the membrane is introduced, which keeps the membrane morphology in a stable or metastable tubular shape, even without the presence of curvature inducing particles[4]. The membrane curvature can therefore be regulated by fixing its reduced volume, with the addition of the contribution of equation 2.1.8 to the energy of the system. The curvature induced by bound particles is expected to depend on the curvature induced by the volume constraint, which in turn affects the membrane-mediated interaction. The values for the equilibrium reduced volume v_0 examined are $v_0 = 0.35$, 0.4, 0.45, 0.5, 0.55, 0.6, 0.65, 0.7 for the tubular morphology, and $v_0 = 0.95$ for the spherical

morphology. It is important to note that the tubule is indeed a metastable morphology for reduced volume constraints smaller than $v_0 = 0.652$, as the stable morphology is either an oblate discocyte or an axisymmetric stomatocyte[4]. In order to prevent the transition to other morphologies, a higher value for the bending rigidity, $\kappa = 30k_BT$, has been chosen[4]. The simulations for $v_0 = 0.95$ use the sphere as starting morphology for the membrane, while all others use spherocylinder as described in section 2.2.1. The total number of particles in the system is $N = 400$, their sizes are either 3 or 4 segments, depending on the simulation. For each simulation, the membrane coverage ratio is kept at either 5%, 10%, or 20% by dynamically varying the value of the adsorption energy U. The adjustment occurs as

$$U \longrightarrow U - c_U \left(N_B - N_0\right)$$

where N_B is the average estimation of bound particles over the last 10^6 MC steps, whereas N_0 is the desired number of bound particles, determined by counting each particle segment as occupying an area $a_p^2\pi/4$ (see equation 2.1.14) on the membrane. Finally, $c_U = 10^{-5}$ has been chosen as proper value for the dynamics of U, so that the number of adsorbed particles only varies by a few units from the desired number. The data for the radial distribution function is only examined after the number of bound particles has stabilized to a neighborhood of the equilibrium value N_0. The radial distribution function is then estimated to be

$$g(r) = \frac{\rho_1(r)}{\rho_2(r)} \tag{5.0.2}$$

where $\rho_1(r)$ is the measured joint distribution function for finding a particle at distance r from a particle at a properly chosen origin point on the tubule[7], whereas the function $\rho_2(r)$ is the expected joint distribution for a free gas of particles with the same hard-core shape. The distribution of a simple free gas is not correct as the particles in this project are rigid bodies with spacial extension.

The function $\rho_1(r)$ is estimated as the distribution of the distances between all pairs of particles for which at least one particle is central. Central particles are defined to be particles bound to the central 50% area of the tubule. Therefore, in the case of tubular structures, they exclude the particles bound to the spherical ends, that is, areas with a different membrane curvature. The axis upon which the central particles are determined is the first principal component of the covariance matrix of the spatial distribution of membrane vertices. The pairs are collected at different points in time, at intervals of 100 MC steps per vertex for a period of around $\approx 10^7$ MC steps per vertex.

For symmetric particles on a planar surface it is expected to be $\rho_2(r) = 2\pi r$ for r larger than the hardcore diameter. The fact that our particles are not symmetric makes the composition of $\rho_2(r)$ more complicated. The value of function $\rho_2(r)$ for particles of 3 and 4 segments is estimated by running a simulation of randomly positioning flattened particles on a plane with periodic boundary conditions. The flattened particles are analogous to those defined in 2.1.2 with the exception of not being curved, as they lie on a plane. The flattened particle is a line of 3 or 4 points at distance a_p in the sequence,

each having a hard-core radius of $a_p/2$. A simulation is carried out to randomly position the particles in space with random orientation. The relative position of the centers is then measured as the estimation for $\rho_2(r)$. Figure 5.0.1 displays the estimation of the $\rho_2(r)$ functions for particles of sizes 3 and 4. The curves have two non-smooth points, corresponding to the distances at which two particles acquire more rotational freedom. The curves in figure 5.0.1 are identical to $\rho_2(r) = 2\pi r$ for large values of r.

5.1. Radial distribution functions for bound particles

The radial distribution function shows that the correlation at short distance is the strongest for membranes of reduced volume of $v_0 = 0.95$, whereas the minimal steepness is for membranes with reduced volume of $v_0 = 0.35$ and $v_0 = 0.4$, see figures 5.1.1 and 5.1.2. Using equation 5.0.1 to derive the equivalent particle-particle interaction energy with membrane mediation, the attraction of particles at low range ($1.5\,a_m$ to $3\,a_m$) is stronger for the spherical membrane morphology (reduced volume $v_0 = 0.95$) and for larger tubular morphologies with reduced volume higher than $v_0 = 0.4$. The cases with particles of size 4 and membrane coverage of 10% with reduced volume $v_0 = 0.7$, and membrane coverage of 20% with reduced volumes $v_0 = 0.65$ and $v_0 = 0.7$ had a morphological transition of the membrane into a disk, and have therefore been excluded. The condition $v_0 = 0.327$ is expected to create membranes with radius length closest to r_p, defined in equation A.1.1. Indeed, if the volume of the membrane is calculated under the assumption that the membrane shape is a spherocylinder, one gets

$$4\pi r_p^2 + 2\pi h r_p = A, \tag{5.1.1}$$

$$\frac{4}{3}\pi r_p^3 + \pi h r_p^2 = V. \tag{5.1.2}$$

Solving equation 5.1.1 for h and substituting in equation 5.1.2, with the value $A = A_0$ as defined in 2.1.6, gives approximately $v_0 \approx 0.32689$. As a consequence of the definition of membrane-particle interaction in equation 2.1.11, the radius r_p is the most compatible curvature for a tubule to bind with the particle models used in this project. The membrane-mediated interaction due to the bending energy cost is therefore expected to be minimized for membranes of reduced volume $v_0 = 0.327$. It is no surprise that both membranes of reduced volume $v_0 = 0.35$ and $v_0 = 0.4$ show the smallest attraction at short distance between particles. The reduced volumes of $v_0 = 0.45$ up to $v_0 = 0.7$, together with $v_0 = 0.95$ show an increasing stronger interaction energy at low ranges for all membrane coverages and both particle sizes, see figures 5.1.3 and 5.1.4.

The total interaction between particles of size 4 on the membrane with reduced volume $v_0 = 0.95$ shows a second minimum for membrane coverages of 10% and 20% for $r = 3.5a_m$ to $4a_m$, see figures 5.1.4(b) and 5.1.4(c). This corresponds to the effect of the second coordination in the lines of side-by-side particle alignments, see figures 5.1.6(e) and 5.1.6(f). In the range from $r = 3.2a_m$ to $4.5a_m$ for the membrane with reduced volume $V_0 = 0.95$ and coverage of 5% the energy curve appears less steep, see figure

a)

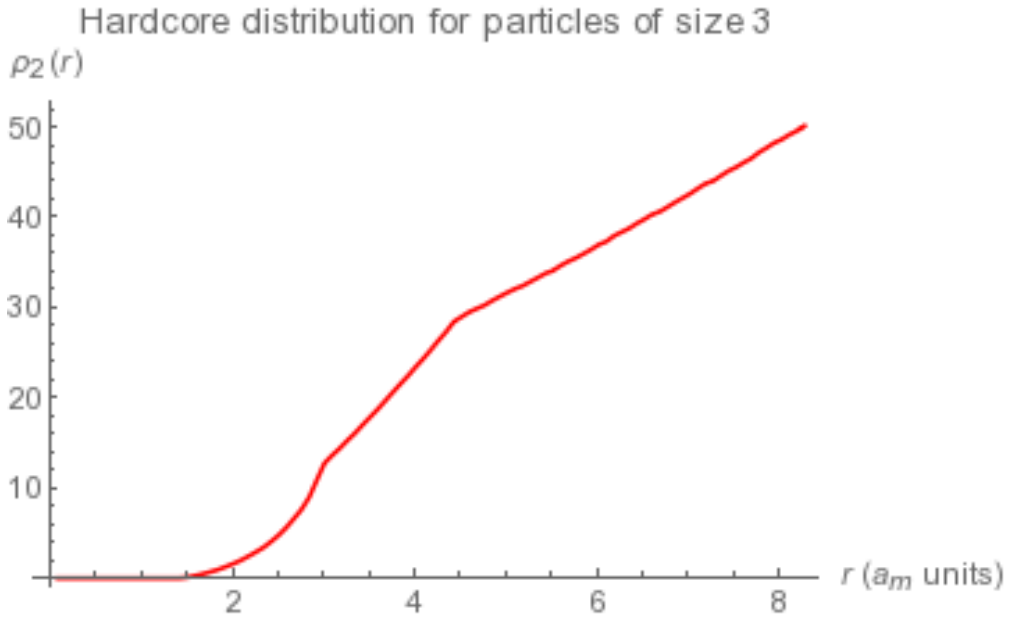

b)

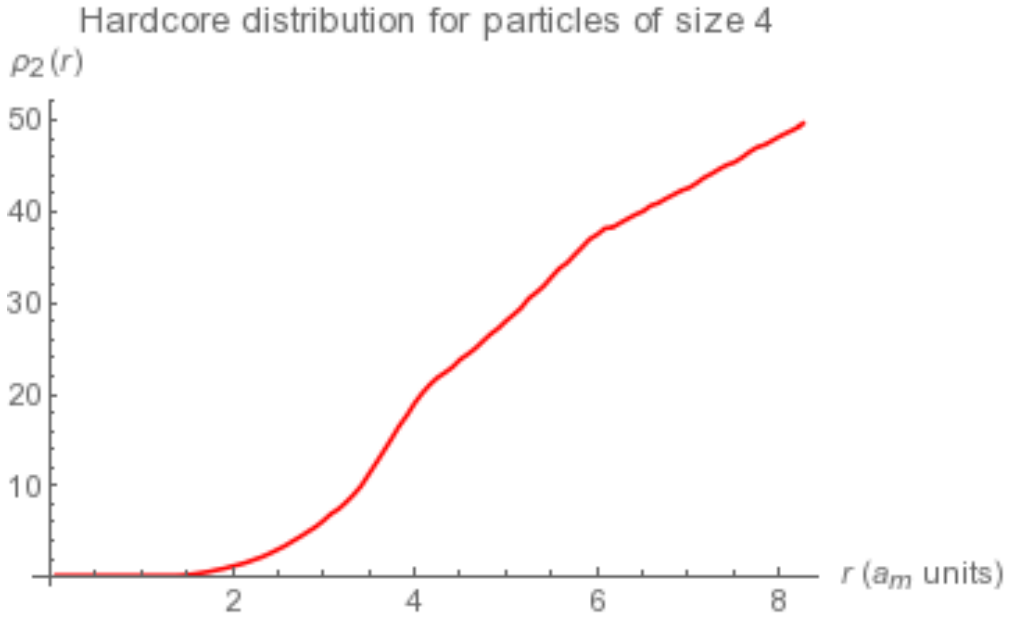

Figure 5.0.1.: Distribution functions $\rho_2(r)$ for a free gas of particles of size 3 (a) and 4 (b), on a plane with toroidal boundary conditions. In both graphs there are two non-smooth points on the curves. The first non-smooth point corresponds to the distance of full rotational freedom for particles at the side of a reference particle ($3\,a_m$ for particles of three segments, $\frac{3\sqrt{35}}{4}\,a_m \approx 4.437\,a_m$ for particles of four segments), while the second non-smooth point corresponds to the distance of full rotational freedom for particles at the top of a reference particle ($4.5\,a_m$ for particles of three segments, $6\,a_m$ for particles of four segments). Notice that after the last non-smooth points the curves are described by $\rho_2(r) = 2\pi r$.

5.1.4(a), this can again be reconnected to the formation of lines of particles, see figure 5.1.6(d).

a)

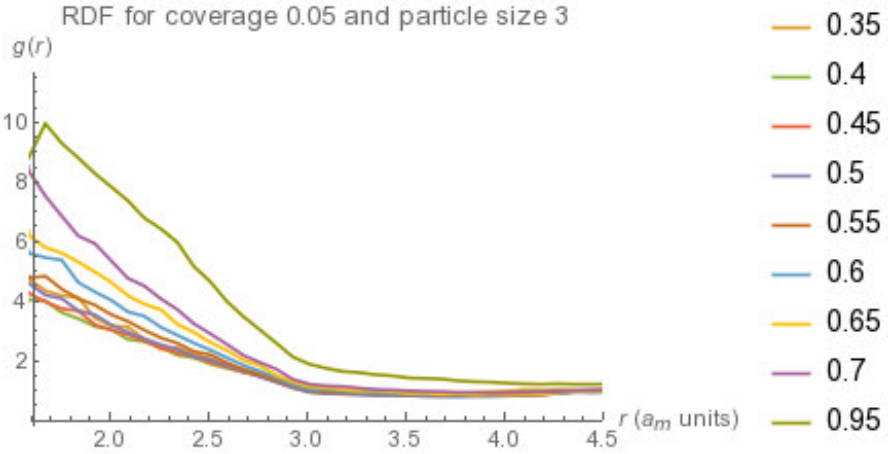

b)

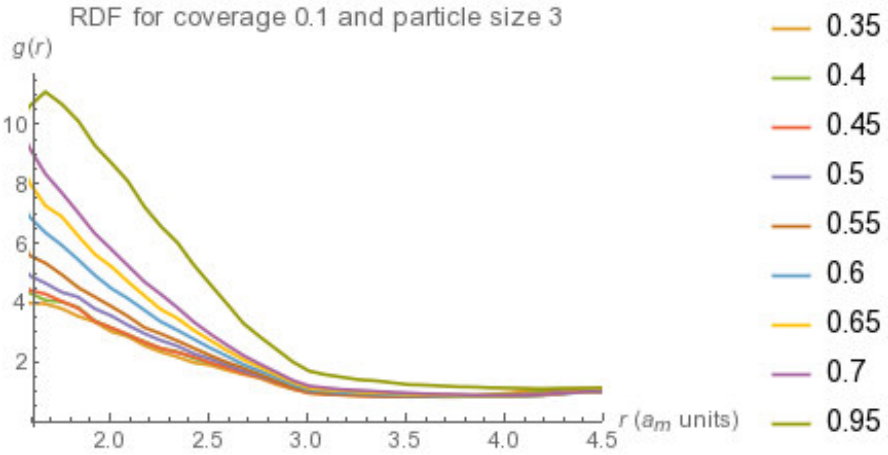

c)

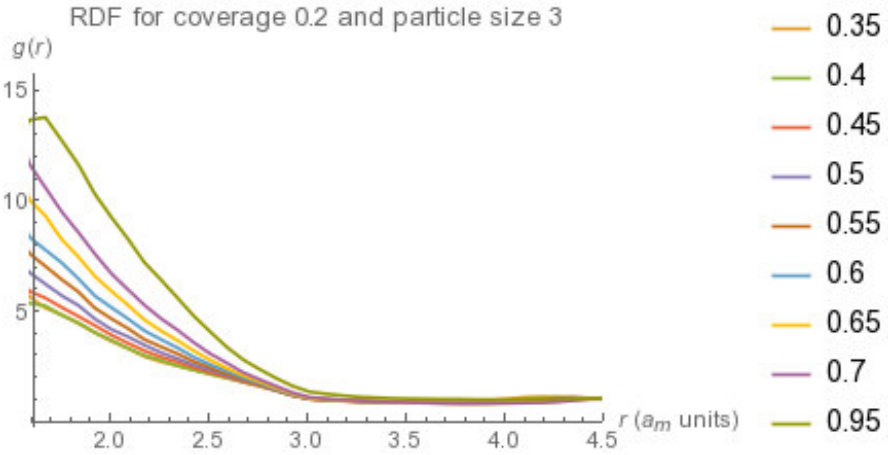

Figure 5.1.1.: Radial distribution functions for particles of size 3 bound to the membrane. The rows correspond to membrane coverages of 0.05 (a), 0.1 (b), and 0.2 (c). The strongest correlation at low distance has been observed for reduced volume $v_0 = 0.95$.

a)

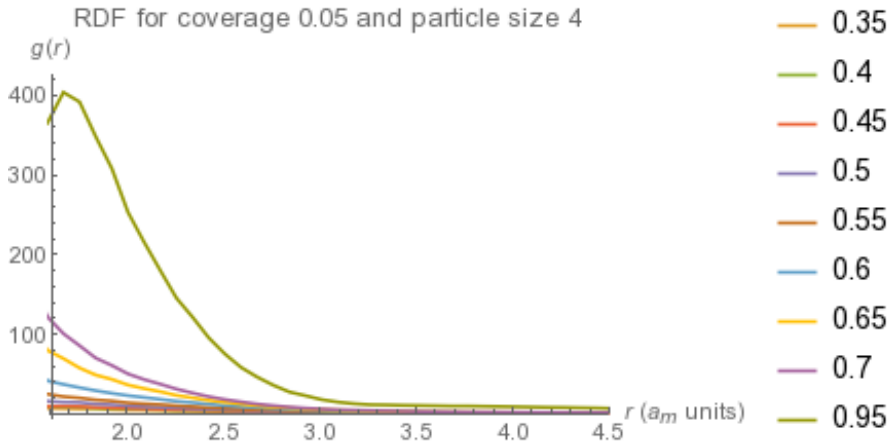

b)

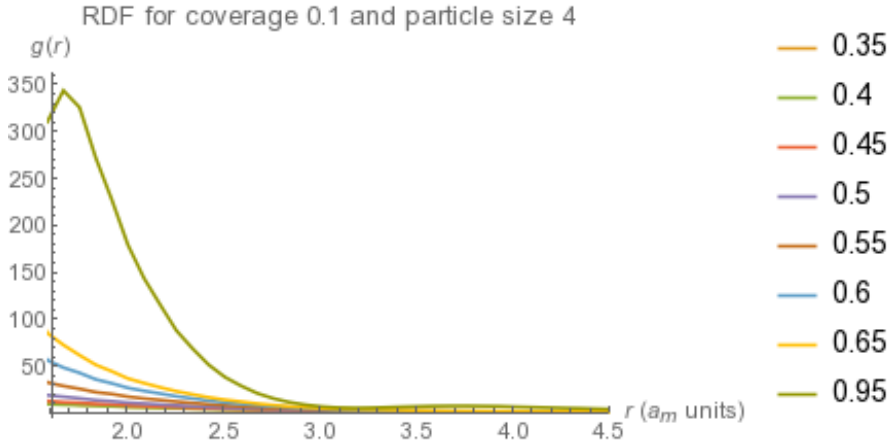

c)

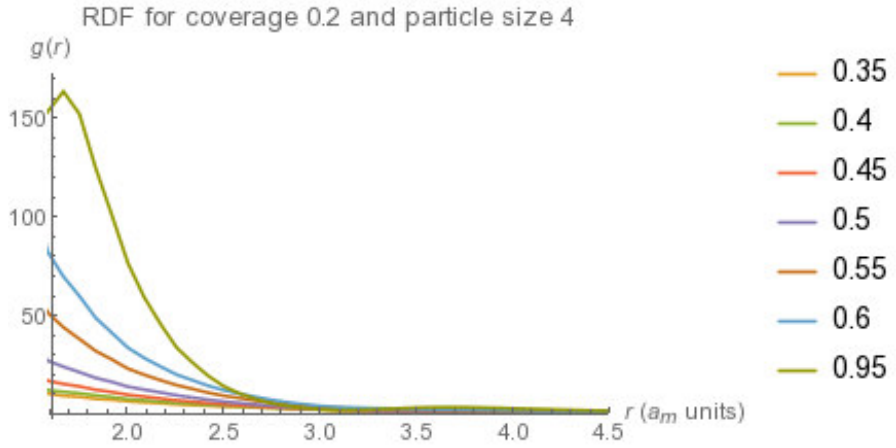

Figure 5.1.2.: Radial distribution functions for particles of size 4 bound to the membrane. The rows correspond to membrane coverages of 0.05 (a), 0.1 (b), and 0.2 (c). The strongest correlation at low distance has been observed for reduced volume $v_0 = 0.95$.

a)

b)

c)

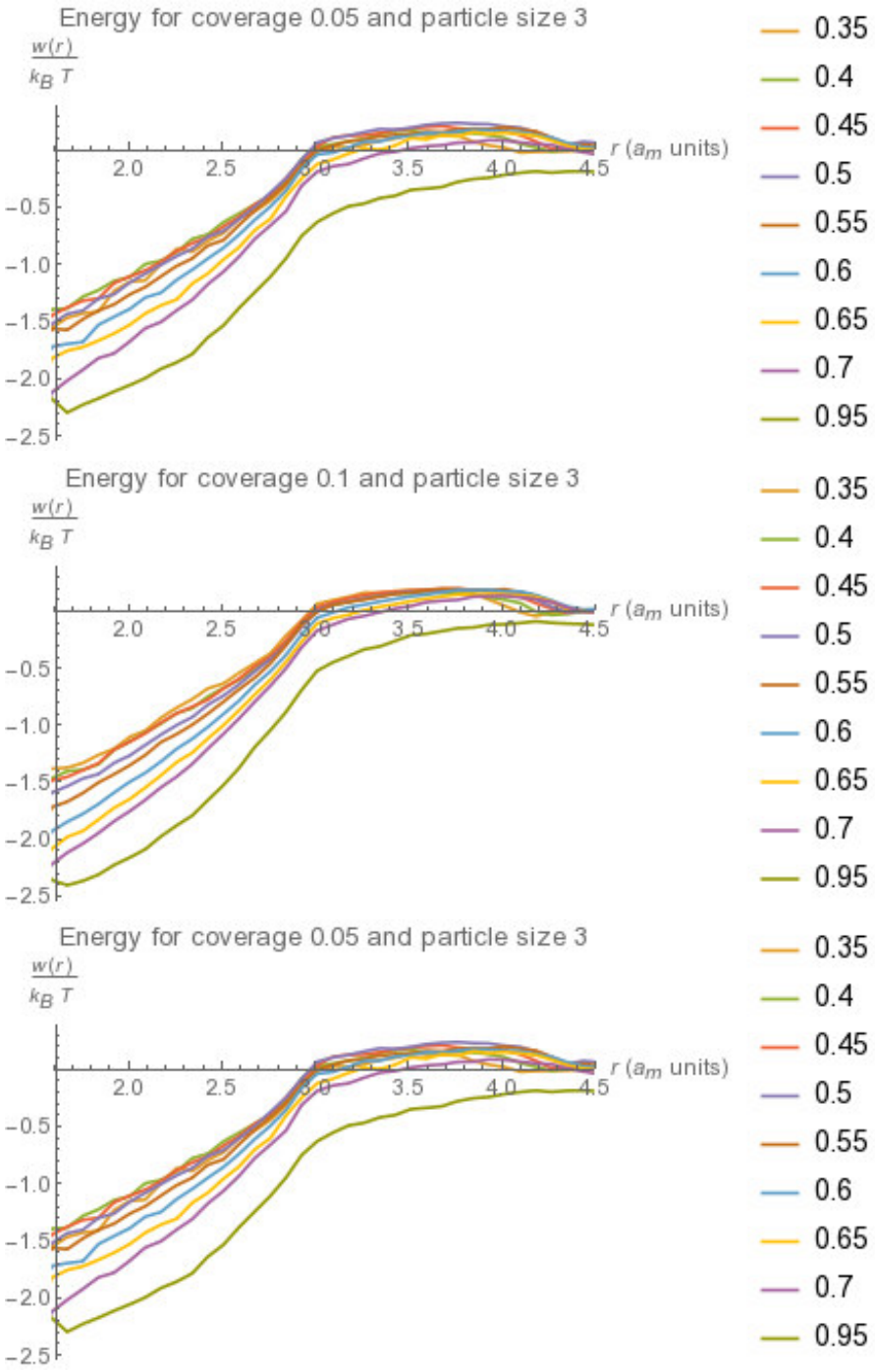

Figure 5.1.3.: Membrane-mediated interaction energies for particles of size 3 bound to the membrane. The rows correspond to membrane coverages of 0.05 (a), 0.1 (b), and 0.2 (c).

a)

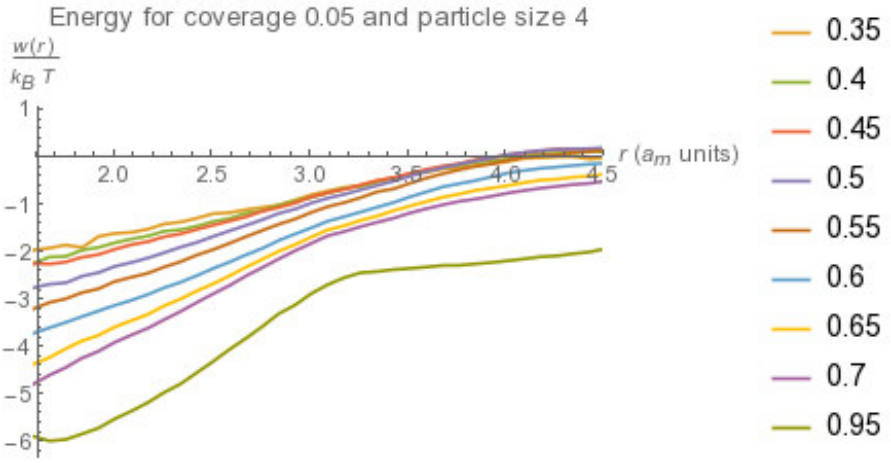

b)

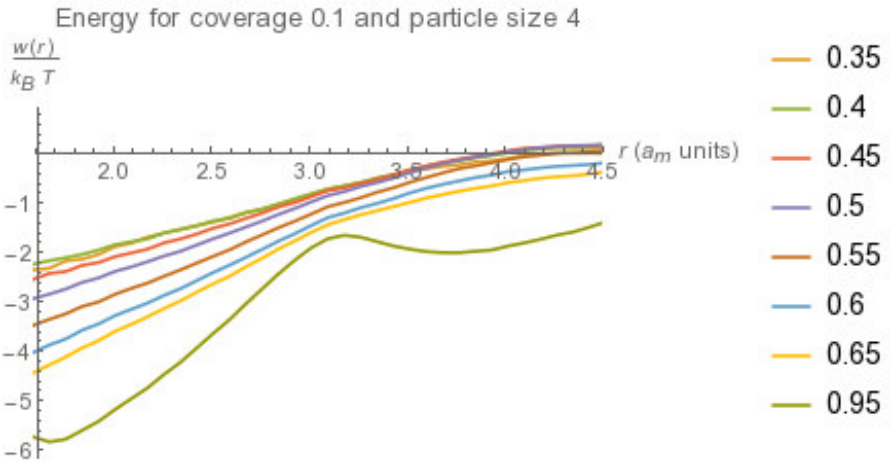

c)

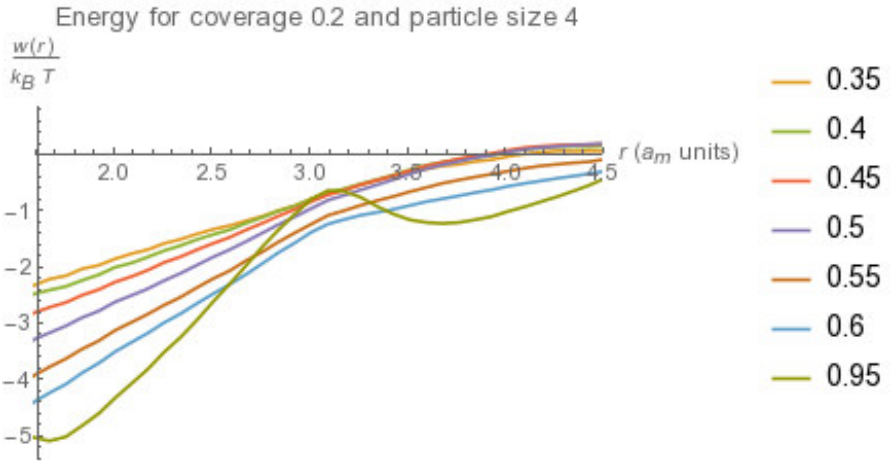

Figure 5.1.4.: Membrane-mediated interaction energies for particles of size 4 bound to the membrane. The rows correspond to membrane coverages of 0.05 (a), 0.1 (b), and 0.2 (c).

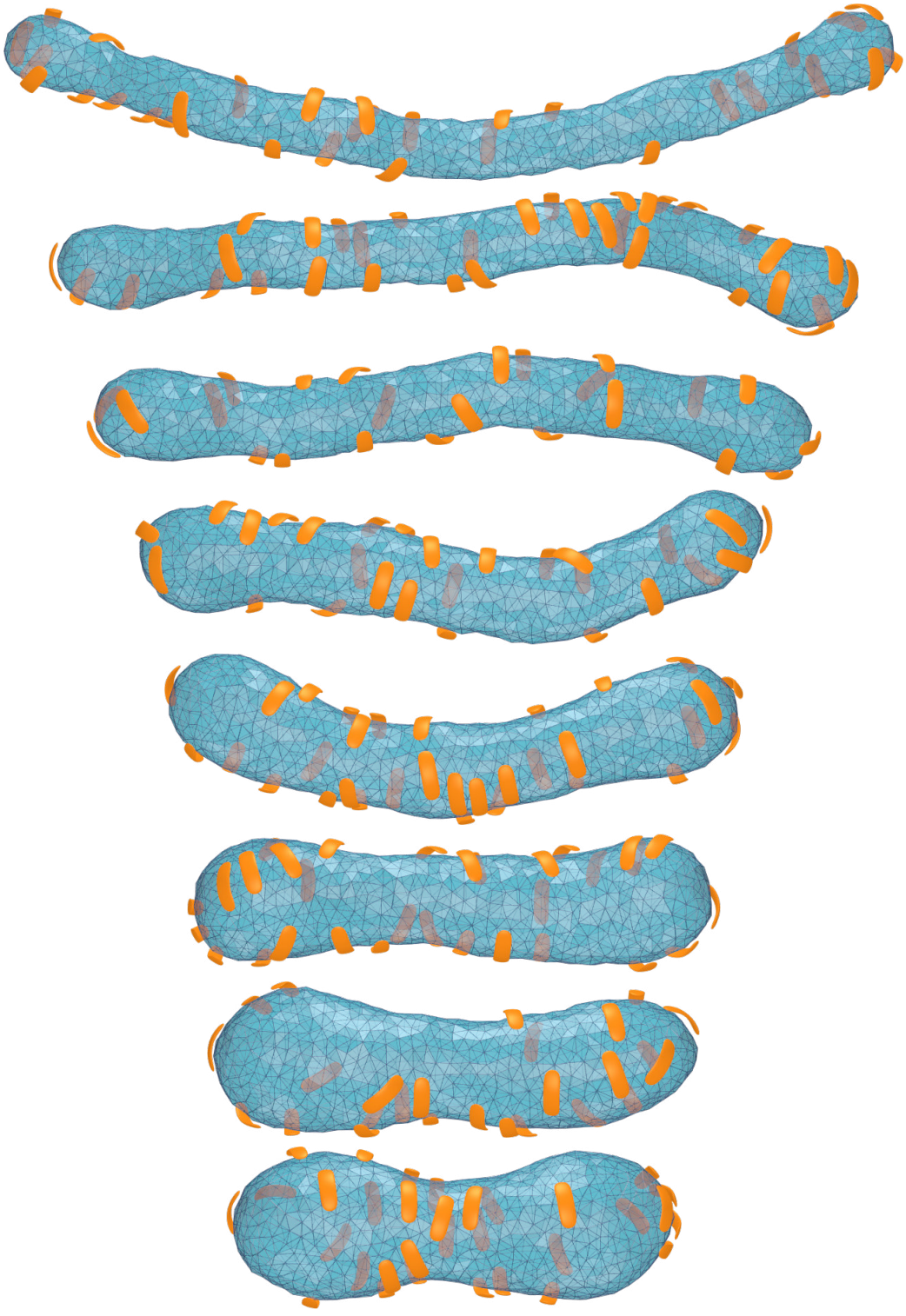

Figure 5.1.5.: Comparison of tubular morphologies with different reduced volumes. The membrane coverage is 10% and the particles have three segments. The reduced volume is constrained to $v_0 = 0.35$, 0.4, 0.45, 0.5, 0.55, 0.6, 0.65, 0.7 for (a,b,c,d,e,f,g,h), respectively.

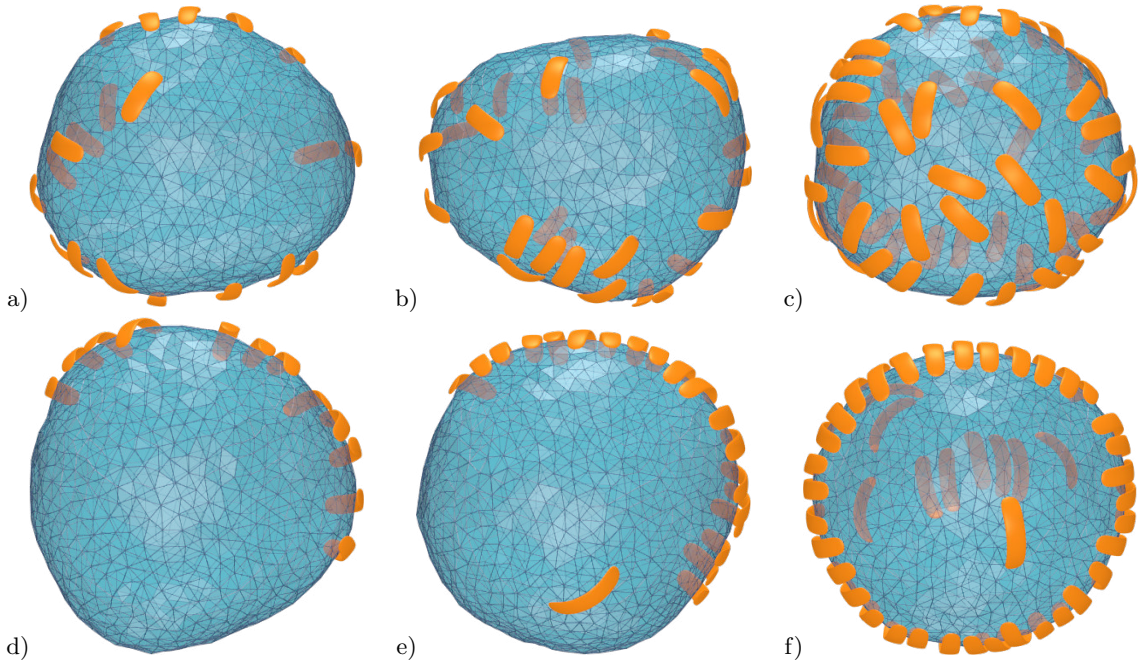

Figure 5.1.6.: Exemplary morphologies with reduced volume constrained to $v_0 = 0.95$ for particles of size 3 and 4 at different membrane coverages. The morphology is spherical. The rows (a, b, c) and (d, e, f) display snapshots of the membrane with bound particles of sizes 3 and 4, respectively. The columns (a, d), (b, e), and (c, f) correspond to membrane coverages of 5%, 10%, and 20%, respectively. Notice that (e) and (f) present lines of side-by-side aligned particles, which is compatible with the second coordination location visible in the potential in figures 5.1.3(d) and 5.1.3(f).

A. Appendix

A.1. Initial membrane morphologies

In order to perform simulations with all different initial membrane configurations, the membrane has been shaped into a disk and a spherocylinder by adding a squeezing potential to the spherical configuration. That is, starting from the spherical configuration, a MC simulation has been performed with vertex movements and edge flips, until the desired shape has been reached. At this point, simulated annealing (i.e. a decrease of temperature in the MC acceptance ratio) is performed to smoothen the surface. Given the radius of curvature R_p of the particles, as defined in 2.1.9, and the membrane-particle interaction potential described in equation 2.1.12, the ideal matching radius for the membrane is determined to be

$$r_p = R_p - \frac{r_1 + r_2}{2} \tag{A.1.1}$$

- For the disk, a radial potential around the z-axis is applied, which is minimized in equations 2.2.3. The value of r is replaced by r_p, and R is calculated so that the area of the disk is A_{ref}.

- In order to shape the membrane into a spherocylinder, a semi-harmonic potential is created for vertices in the triangulated surface depending on their distance to the z-axis. The semi-harmonic potential is

  $$c(r_z - r)^2 \Theta(r_z - r)$$

  where r_z is the distance to the z-axis, c is a tunable constant and Θ is the Heaviside step function.

  In order to accelerate the process an additional pulling potential is created to stretch the membrane along the z-axis until a reasonable length has been reached.

A.2. Rotations with quaternions

A computationally efficient implementation of rotations can be achieved with the representation of rotations in quaternion algebra[16]. Quaternions are extensions of complex numbers that have three different kinds of imaginary parts:

$$\mathbf{q} = a + \mathbf{i}b + \mathbf{j}c + \mathbf{k}d$$

Under multiplication the imaginary symbols follow the rules:

$$\begin{array}{lll} \mathbf{ij} = \mathbf{k} & \mathbf{jk} = \mathbf{i} & \mathbf{ki} = \mathbf{j} \\ \mathbf{i}^2 = -1 & \mathbf{j}^2 = -1 & \mathbf{k}^2 = -1 \end{array}.$$

Unit quaternions, that is quaternions whose components observe $a^2 + b^2 + c^2 + d^2 = 1$ may be employed to represent rotations, by acting on vectors by

$$\mathbf{p}' = \mathbf{q} \cdot \mathbf{p} \cdot \mathbf{q}^{-1},$$

where p is in the form $p_x\mathbf{i} + p_y\mathbf{j} + p_z\mathbf{k}$. The correspondence between a unit quaternion and the axis-angle ($\mathbf{r}$, θ) representation of a rotation is given by:

$$\mathbf{q} = \cos\frac{\theta}{2} + \mathbf{r}\sin\frac{\theta}{2}, \tag{A.2.1}$$

where $\mathbf{r} = r_x\mathbf{i} + r_y\mathbf{j} + r_z\mathbf{k}$ is the axis of rotation and θ is the rotation angle.

Small random rotations can therefore be performed by picking a random unit quaternion $\mathbf{q}_\varepsilon$ in the neighborhood of 1, such that the Euclidean distance to unity is less than ε. Given a random uniformly distributed unit quaternion $\mathbf{q}$, a suitable neighborhood of unity can be found by[16]

$$\mathbf{q}_\varepsilon = \frac{1 + \varepsilon\mathbf{q}}{\|1 + \varepsilon\mathbf{q}\|}, \tag{A.2.2}$$

where ε is the rotational magnitude tuning parameter.

In order to generate random unit quaternions, an algorithm originally developed by Marsaglia has been used[56, 30]. The procedure is as follows: generate numbers x_1 and x_2 independent and uniform in the interval $[-1, 1]$, such that $S_1 = x_1^2 + x_2^2 < 1$. The same procedure is repeated to generate numbers x_3 and x_4 independent and uniform in the interval $[-1, 1]$, such that $S_2 = x_3^2 + x_4^2 < 1$. After calculating $c = \sqrt{\frac{1-S_1}{S_2}}$, the random unit quaternion will be $\mathbf{q} = (x_1, x_2, c \cdot x_3, c \cdot x_4)$. The distribution of rotation axes is uniform (because of symmetry). The distribution of angles on the other hand is non-uniform and slanted towards $\theta_{\max}$. For a given ε, the maximum angle is $\theta_{\max} = 2\arccos\sqrt{1 - \varepsilon^2}$. The value $\varepsilon = 0.02$ has been employed throughout this project.

A.3. Radii of tubules and disks

Triangulated membranes of tubular shapes can be characterized by their radius. Similarly, disk-like shapes vary in thickness. These quantities can be extracted from the triangulated structure of the model membrane. The thickness of disks can be defined as the distance between the two sheets at the center of mass of the disk. For an ideal disk, the two sheets are parallel and their distance is equal to $2R_p$, where R_p is the curvature radius of the particles. In reality, the results of the simulations show that disks tend to bulge slightly and the size of particles influences the thickness.

A geometrical method has been devised to estimate these quantities. Namely, for every vertex of the membrane i, a vertex $j(i)$ opposite to i with respect to the center

of mass is associated. Formally, by calling $\mathbf{p}_i$ the position with respect to the center of mass of vertex i of the membrane, the vertex $j(i)$ is the one such that $\frac{\mathbf{p}_i \cdot \mathbf{p}_{j(i)}}{|\mathbf{p}_i||\mathbf{p}_{j(i)}|}$ is minimal, which means as close to negative unity as possible. The vertex $j(i)$ will be located close to the antipodal position on the membrane to the vertex i. By calling the set of such pairs $X = \{i, j(i)\}_{i \in \text{vertices}}$, the estimate for the tubular radius and the discoidal thickness is given by the expression $\min \{|p_i - p_j|\}_{i,j \in X}$, that is, the minimum of the distances of vertex pairs in set X.

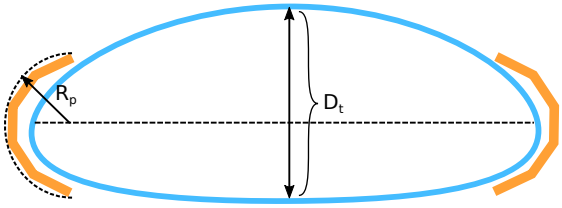

Figure A.3.1.: Schematic view of the disk thickness at its center.

A.4. Bending energy of ideal shapes

The bending energy of membranes given by equations 1.2.5 can be solved for ideal shapes of tubules and disks as parametrized in section 2.2.1 .

A.4.1. Tubule

The ideal tubule is modeled as a spherocylinder, which is a cylinder (of height h and radius r) capped with two semispheres of radius r. The computed bending energy is

$$E_t = \pi\kappa \left(8 + \frac{h}{r}\right).$$

This equation can be expressed as a function of r by inverting it with the area equation

$$A_t = 4\pi r^2 + 2\pi h r$$

therefore

$$E_t = 6\pi\kappa + \frac{3^{2/3} \sqrt[3]{\frac{\pi}{2}} \kappa}{r^2}$$

A.4.2. Disk

The ideal disk is a cylinder of height $2r$ and radius R, whose curved surface is capped by an outer semi-torus parametrized by r and R. The bending energy is given only by the curved region of the surface. A parametrization of the outer semi-torus with angles θ and ϕ is introduced, where $\theta \in (-\frac{\pi}{2}, \frac{\pi}{2})$ spans the section of radius r, while $\phi \in (0, 2\pi)$ revolves around the rotational symmetry axis of the disk.

Bending energy

The equation 1.2.5 is solveable for the disk. The area element for the torus is

$$dA = r(R + r\cos\theta)\, d\theta\, d\phi$$

and the mean curvature is given by

$$H = \frac{1}{2}\left(\frac{1}{r} + \frac{\cos\theta}{R + r\cos\theta}\right).$$

At this point, equation 1.2.5 is expressed as

$$E_d = \frac{1}{2}\kappa \int_0^{2\pi} \int_{-\frac{\pi}{2}}^{\frac{\pi}{2}} \left(\frac{1}{r} + \frac{\cos\theta}{R + r\cos\theta}\right)^2 r(R + r\cos\theta)\, d\phi\, d\theta,$$

which results in

$$E_d = 4\pi\kappa \left(\frac{R^2 \left(4\tanh^{-1}\left(\frac{R-r}{\sqrt{(r-R)(r+R)}}\right) + 5\tanh^{-1}\left(\sqrt{\frac{2r}{r+R} - 1}\right)\right)}{r\sqrt{(r-R)(r+R)}} + 2 \right).$$

Area of the disk

The area of the disk can be calculated by integrating or by using Pappus' theorem, resulting in

$$A_d = 4\pi r^2 + 2\pi^2 rR + 2\pi R^2.$$

By inverting the area equation, under the assumption of constant membrane area, it is possible to express the bending energy as a function of r only

$$E_d = \frac{\sqrt{2}\pi^{2/3}\kappa \left(A - \pi^{4/3} r\right)^2 (X + Y)}{r\sqrt{\pi^{2/3} r \left(\pi^{2/3} A - (\pi^2 - 6)\, r\right) - 6^{2/3}}} + 8\pi\kappa,$$

where

$$X = 4\tanh^{-1}\left(\frac{A - \sqrt[3]{\pi}(2 + \pi) r}{\sqrt{2\pi^{4/3} A r - 2\pi^{2/3}\left(\pi^2 - 6\right) r^2 - 2\ 6^{2/3}}}\right),$$

$$Y = 5\tanh^{-1}\left(\sqrt{-\frac{4\sqrt[3]{\pi} r}{(\pi - 2)\sqrt[3]{\pi} r - A} - 1}\right),$$

and $A = \sqrt{\pi^{2/3}\left(\pi^2 - 8\right) r^2 + 2\ 6^{2/3}}$ is a repeated subexpression.

A.5. Radial distribution of an ideal gas on a cylinder

In this section the radial distribution function for a free gas on an infinite cylinder is computed. Under the assumption of constant surface density ρ for particles of a free gas, the expected density at distance R from a point on the cylinder can be described as the area of the cylinder inside a sphere of radius R having its center on the cylinder. The cylinder is represented by the implicit parametrization

$$x^2 + y^2 = r^2, \tag{A.5.1}$$

while the sphere with center on the edge of the cylinder at $(r, 0, 0)$ and radius R is given by

$$(x - r)^2 + y^2 + z^2 = R^2. \tag{A.5.2}$$

In what follows, the intersection curve between the cylinder (A.5.1) and the sphere (A.5.2) is parametrized with polar coordinates in the xy-plane. The surface area of the cylinder that lies inside the sphere is calculated by solving A.5.2 for z, for any sphere of size R, giving

$$\begin{cases} x = & r\cos\phi \\ y = & r\sin\phi \\ z = & \sqrt{R^2 + 2r^2(\cos\phi - 1)} \end{cases}. \tag{A.5.3}$$

The area element for the integration on a cylindrical surface is $dA = r\,dz\,d\phi$. At this point, by calling $B = \sqrt{R^2 + 2r^2(\cos\phi - 1)}$, one derives

$$\int_{-A}^{A}\int_{-B}^{B} r\,dz\,d\phi, \tag{A.5.4}$$

where B is the integration boundary along the z axis, while A is the maximum value of ϕ for a given value of R. This integral can be divided in two parts, the case in which the sphere does not envelope the entire cylindrical section (i.e. $R < 2r$) and the case in which it does (i.e. $R > 2r$). For the first case, the value $A = \arccos(\frac{R^2-2r^2}{2r})$ is replaced in equation A.5.4. Solving the integral, the result is

$$8 \cdot r \cdot R \cdot \mathrm{E}\left(\frac{1}{2}\arccos\left(\frac{2r^2 - R^2}{2r^2}\right)|\frac{4r^2}{R^2}\right), \tag{A.5.5}$$

where $E(a, b)$ is the incomplete elliptic integral of the second kind, given by

$$\mathrm{E}(a|b) = \int_0^a \sqrt{1 - b\sin x}\,dx.$$

For the second case, the angular integration occurs around the whole cylinder, therefore $A = \pi$. Setting up the limiting cases

$$\int_{-\pi}^{\pi}\int_{-B}^{B} r\,dz\,d\phi,$$

which results in

$$8r\sqrt{R^2-4r^2}\mathrm{E}\left(-\frac{4r^2}{R^2-4r^2}\right), \tag{A.5.6}$$

where $\mathrm{E}(b)$ is the complete elliptic integral of the second kind

$$\mathrm{E}(b) = \mathrm{E}\left(\frac{\pi}{2}|\mathrm{b}\right) = \int_0^{\frac{\pi}{2}} \sqrt{1-b\sin x}\,dx.$$

In order to get the radial distribution function, the formulae A.5.5 and A.5.6 are derived by R, resulting in

$$\begin{cases} 8\cdot r\cdot \mathrm{F}\left(\frac{1}{2}\arccos\left(1-\frac{R^2}{2r^2}\right)|\frac{4r^2}{R^2}\right) & \text{if } R<2r \\ \frac{8\cdot r\cdot R\cdot \mathrm{K}\left(-\frac{4r^2}{R^2-4r^2}\right)}{\sqrt{R^2-4r^2}} & \text{if } R>2r \end{cases},$$

where $F(a,b)$ is the incomplete elliptic integral of the first kind

$$\mathrm{F}(a|b) = \int_0^a \frac{1}{\sqrt{1-b\sin^2 x}}\,dx$$

and $K(a)$ is the complete elliptic integral of the first kind

$$\mathrm{K}(b) = \mathrm{F}\left(\frac{\pi}{2}|b\right).$$

Bibliography

[1] Julia Adam, Nirakar Basnet, and Naoko Mizuno. Structural insights into the cooperative remodeling of membranes by amphiphysin/bin1. *Sci Rep*, 5:15452, 2015.

[2] Gary S Ayton, Philip D Blood, and Gregory A Voth. Membrane remodeling from N-BAR domain interactions: insights from multi-scale simulation. *Biophys J*, 92(10):3595–602, May 2007.

[3] Gary S. Ayton, Edward Lyman, Vinod Krishna, Richard D. Swenson, Carsten Mim, Vinzenz M. Unger, and Gregory A. Voth. New insights into BAR domain-induced membrane remodeling. *Biophys. J.*, 97(6):1616–1625, September 2009.

[4] Amir Houshang Bahrami and Gerhard Hummer. Formation and stability of lipid membrane nanotubes. *ACS nano*, 11(9):9558–9565, 2017.

[5] Amir Houshang Bahrami, Reinhard Lipowsky, and Thomas R. Weikl. Tubulation and aggregation of spherical nanoparticles adsorbed on vesicles. *Phys. Rev. Lett.*, 109:188102, 2012.

[6] Anne-Florence Bitbol, Paul G Dommersnes, and Jean-Baptiste Fournier. Fluctuations of the casimir-like force between two membrane inclusions. *Physical Review E*, 81(5):050903, 2010.

[7] David Chandler and Jerome K Percus. Introduction to modern statistical mechanics. *Physics Today*, 41:114, 1988.

[8] S. Chen, T. Desai, J. A. McNew, P. Gerard, P. J. Novick, and S. Ferro-Novick. Lunapark stabilizes nascent three-way junctions in the endoplasmic reticulum. *Proc Natl Acad Sci USA*, 2015.

[9] S. Chen, P. Novick, and S. Ferro-Novick. Er network formation requires a balance of the dynamin-like gtpase sey1p and the lunapark family member lnp1p. *Nat Cell Biol*, pages 707–716, 2012.

[10] James Frederic Danielli and Hugh Davson. A contribution to the theory of permeability of thin films. *Journal of Cellular Physiology*, 1935.

[11] Bertram Daum, Andrea Auerswald, Tobias Gruber, Gerd Hause, Jochen Balbach, Werner Kühlbrandt, and Annette Meister. Supramolecular organization of the human N-BAR domain in shaping the sarcolemma membrane. *J. Struct. Biol.*, 194(3):375–382, Jun 2016.

[12] Rumiana Dimova. Recent developments in the field of bending rigidity measurements on membranes. *Adv. Colloid Interface Sci.*, 208:225–234, Jun 2014.

[13] PG Dommersnes and J-B Fournier. N-body study of anisotropic membrane inclusions: Membrane mediated interactions and ordered aggregation. *The European Physical Journal B-Condensed Matter and Complex Systems*, 12(1):9–12, 1999.

[14] M. Terasaki et al. Stacked endoplasmic reticulum sheets are connected by helicoidal membrane motifs. *Cell*, 2013.

[15] R. Fernández-Busnadiego, Y. Saheki, and P. De Camilli. Three-dimensional architecture of extended synaptotagmin-mediated endoplasmic reticulum-plasma membrane contact sites. *Proc. Natl. Acad. Sci. U.S.A.*, 2015.

[16] D. Frenkel and B. Smit. *Understanding molecular simulation: from algorithms to applications*, volume 1. Academic press, 2001.

[17] Adam Frost, Rushika Perera, Aurélien Roux, Krasimir Spasov, Olivier Destaing, Edward H Egelman, Pietro De Camilli, and Vinzenz M Unger. Structural basis of membrane invagination by f-bar domains. *Cell*, 132(5):807–17, Mar 2008.

[18] Gerhard Gompper and Daniel M. Kroll. Network models of fluid, hexatic and polymerized membranes. *Journal of Physics: Condensed Matter*, 9:8795–8834, 1997.

[19] E. Gorter and F. Grendel. On bimolecular layers of lipoids on the chromocytes of the blood. *Journal of Experimental Medicine*, 1925.

[20] M Goulian, R Bruinsma, and P Pincus. Long-range forces in heterogeneous fluid membranes. *EPL (Europhysics Letters)*, 22(2):145, 1993.

[21] Wolfgang Helfrich. Elastic Properties of Lipid Bilayers: Theory and Possible Experiments. *Z Naturforsch C*, 28(11):693–703, Nov-Dec 1973.

[22] M. W. Hetzer. The nuclear envelope. *Cold Spring Harb. Perspect. Biol.*, 2, 2010.

[23] Junjie Hu, Yoko Shibata, Christiane Voss, Tom Shemesh, Zongli Li, Margaret Coughlin, Michael M Kozlov, Tom A Rapoport, and William A Prinz. Membrane proteins of the endoplasmic reticulum induce high-curvature tubules. *Science (New York, N.Y.)*, 319(5867):1247–50, Feb 2008.

[24] F Jülicher. The morphology of vesicles of higher topological genus: Conformal degeneracy and conformal modes. *J. Phys. II*, 6:1797–1824, December 1996.

[25] K S Kim, J Neu, and G Oster. Effect of protein shape on multibody interactions between membrane inclusions. *Phys. Rev. E*, 61(4 Pt B):4281–5, Apr 2000.

[26] Michael M Kozlov, Felix Campelo, Nicole Liska, Leonid V Chernomordik, Siewert J Marrink, and Harvey T McMahon. Mechanisms shaping cell membranes. *Current opinion in cell biology*, 29:53–60, Aug 2014.

[27] Hsiang-Ku Lin, Roya Zandi, Umar Mohideen, and Leonid P Pryadko. Fluctuation-induced forces between inclusions in a fluid membrane under tension. *Physical review letters*, 107(22):228104, 2011.

[28] Reinhard Lipowsky. The conformation of membranes. *Nature*, 349(6309):475, 1991.

[29] Reinhard Lipowsky, Martin Brinkmann, Rumiana Dimova, Thomas Franke, Jan Kierfeld, and Xinzhao Zhang. Droplets, bubbles, and vesicles at chemically structured surfaces. *Journal of Physics: Condensed Matter*, 17, 2005.

[30] George Marsaglia. Choosing a point from the surface of a sphere. *The Annals of Mathematical Statistics*, 43:645–646, 1972.

[31] Michitaka Masuda and Naoki Mochizuki. Structural characteristics of BAR domain superfamily to sculpt the membrane. *Semin. Cell Dev. Biol.*, 21(4):391–398, June 2010.

[32] Harvey T McMahon and Jennifer L Gallop. Membrane curvature and mechanisms of dynamic cell membrane remodelling. *Nature*, 438(7068):590, 2005.

[33] Carsten Mim, Haosheng Cui, Joseph A Gawronski-Salerno, Adam Frost, Edward Lyman, Gregory A Voth, and Vinzenz M Unger. Structural basis of membrane bending by the n-bar protein endophilin. *Cell*, 149(1):137–45, Mar 2012.

[34] Jonathon Nixon-Abell, Christopher J. Obara, Aubrey V. Weigel, Dong Li, Wesley R. Legant, C. Shan Xu, H. Amalia Pasolli, Kirsten Harvey, Harald F. Hess, Eric Betzig, Craig Blackstone, and Jennifer Lippincott-Schwartz. Increased spatiotemporal resolution reveals highly dynamic dense tubular matrices in the peripheral er. *Science*, 354, October 2016.

[35] Hiroshi Noguchi. Formation of polyhedral vesicles and polygonal membrane tubes induced by banana-shaped proteins. *J. Chem. Phys.*, 143(24):243109, Dec 2015.

[36] Hiroshi Noguchi. Membrane tubule formation by banana-shaped proteins with or without transient network structure. *Sci. Rep.*, 6(20935):20935, February 2016.

[37] Brian J Peter, Helen M Kent, Ian G Mills, Yvonne Vallis, P Jonathan G Butler, Philip R Evans, and Harvey T McMahon. Bar domains as sensors of membrane curvature: the amphiphysin bar structure. *Science (New York, N.Y.)*, 303(5657):495–9, Jan 2004.

[38] Britta Qualmann, Dennis Koch, and Michael Manfred Kessels. Let's go bananas: revisiting the endocytic BAR code. *Embo J.*, 30(17):3501–3515, August 2011.

[39] N. Ramakrishnan, P. B. Sunil Kumar, and John H. Ipsen. Membrane-mediated aggregation of curvature-inducing nematogens and membrane tubulation. *Biophys. J.*, 104(5):1018–1028, March 2013.

[40] Dianne S Schwarz and Michael D Blower. The endoplasmic reticulum: structure, function and response to cellular signaling. *Cellular and molecular life sciences*, 73(1):79–94, 2016.

[41] Yonatan Schweitzer and Michael M. Kozlov. Membrane-mediated interaction between strongly anisotropic protein scaffolds. *PLoS Comput. Biol.*, 11(2):e1004054, February 2015.

[42] Yonatan Schweitzer, Tom Shemesh, and Michael M. Kozlov. A Model for Shaping Membrane Sheets by Protein Scaffolds. *Biophysical Journal*, 109(3):564–573, August 2015.

[43] U Seifert and R Lipowsky. Morphology of vesicles. *Handbook of biological physics*, 1:403–464, 1995.

[44] U S Seifert, K Berndl, and R Lipowsky. Shape transformations of vesicles: Phase diagram for spontaneous-curvature and bilayer-coupling models. *Phys. Rev. A*, 44(2):1182–1202, Jul 1991.

[45] Udo Seifert. Configurations of fluid membranes and vesicles. *Advances in physics*, 46(1):13–137, 1997.

[46] Tom Shemesh, Robin W. Klemm, and Fabian B. Romano. A model for the generation and interconversion of ER morphologies. *PNAS*, 111 no. 49, 2014.

[47] Y. Shibata, J. Hu, M. M. Kozlov, and T. A. Rapoport. Mechanisms shaping the membranes of cellular organelles. *Annu Rev Cell Dev Biol*, 25, 2009.

[48] Yoko Shibata, Christiane Voss, Julia M Rist, Junjie Hu, Tom A Rapoport, William A Prinz, and Gia K Voeltz. The reticulon and dp1/yop1p proteins form immobile oligomers in the tubular endoplasmic reticulum. *The Journal of biological chemistry*, 283(27):18892–904, Jul 2008.

[49] Mijo Simunovic, Emma Evergren, Ivan Golushko, Coline Prévost, Henri-François Renard, Ludger Johannes, Harvey T McMahon, Vladimir Lorman, Gregory A Voth, and Patricia Bassereau. How curvature-generating proteins build scaffolds on membrane nanotubes. *Proc. Natl. Acad. Sci. USA*, 113(40):11226–11231, Oct 2016.

[50] Mijo Simunovic, Andela Saric, J. Michael Henderson, Ka Yee C. Lee, and Gregory A. Voth. Long-range organization of membrane-curving proteins. *ACS Central Sci.*, 3(12):1246–1253, December 2017.

[51] Mijo Simunovic, Anand Srivastava, and Gregory A. Voth. Linear aggregation of proteins on the membrane as a prelude to membrane remodeling. *Proc. Natl. Acad. Sci. U. S. A.*, 110(51):20396–20401, December 2013.

[52] Mijo Simunovic and Gregory A. Voth. Membrane tension controls the assembly of curvature-generating proteins. *Nat. Commun.*, 6(7219), May 2015.

[53] S. J. Singer and Garth L. Nicolson. The fluid mosaic model of the structure of cell membranes. *Science*, 1972.

[54] K Takei, V I Slepnev, V Haucke, and P De Camilli. Functional partnership between amphiphysin and dynamin in clathrin-mediated endocytosis. *Nature cell biology*, 1(1):33–9, May 1999.

[55] Richard W Tourdot, N Ramakrishnan, and Ravi Radhakrishnan. Defining the free-energy landscape of curvature-inducing proteins on membrane bilayers. *Phys. Rev. E*, 90(2):022717, Aug 2014.

[56] Franz J. Vesely. Angular Monte Carlo integration using quaternion parameters: a spherical reference potential for CCl4. *Journal of Computational Physics*, 47 no. 2:291–296, August 1982.

[57] Gia K Voeltz, William A Prinz, Yoko Shibata, Julia M Rist, and Tom A Rapoport. A class of membrane proteins shaping the tubular endoplasmic reticulum. *Cell*, 124(3):573–86, Feb 2006.

[58] Gia K Voeltz, Melissa M Rolls, and Tom A Rapoport. Structural organization of the endoplasmic reticulum. *EMBO reports*, 3(10):944–950, 2002.

[59] Thomas R Weikl. Membrane-mediated cooperativity of proteins. *Annu. Rev. Phys. Chem.*, Feb 2018.

[60] Shibata Y, Shemesh T, Prinz WA, Palazzo AF, Kozlov MM, and Rapoport TA. Mechanisms determining the morphology of the peripheral er. *Cell*, 2010.

[61] Cem Yolcu and Markus Deserno. Membrane-mediated interactions between rigid inclusions: an effective field theory. *Physical Review E*, 86(3):031906, 2012.

[62] Joshua Zimmerberg and Michael M Kozlov. How proteins produce cellular membrane curvature. *Nature reviews Molecular cell biology*, 7(1):9, 2006.